ABSRACT

Title of thesis: WETTING OF GRAPHENE

Joseph E. Andrews, Master of Science, 2016

Thesis directed by: Professor Siddhartha Das
Department of Mechanical Engineering

Professor Peter W. Chung
Department of Mechanical Engineering

Graphene, a remarkable 2D material, has attracted immense attention for its unique physical properties that make it ideal for a myriad of applications from electronics to biology. Fundamental to many such applications is the interaction of graphene with water, necessitating an understanding of wetting of graphene. Here, molecular dynamics simulations have been employed to understand two fundamental issues of water drop wetting on graphene: (a) the dynamics of graphene wetting and (b) wetting of graphene nanostructures. The first problem unravels that the wetting dynamics of nanodrops on graphene are exactly the same as on standard, non-2D (or non-layered) solids – this is an extremely important finding given the significant difference in the wetting statics of graphene with respect to standard solids stemming from graphene's wetting translucency effect. This same effect, as shown in the second problem, interplays with roughness introduced by nanostructures to trigger graphene superhydrophobicity following a hitherto unknown route.

WETTING OF GRAPHENE

by

Joseph E. Andrews

Thesis submitted to the Faculty of the Graduate School of the
University of Maryland, College Park in partial fulfillment
of the requirements of the degree of
Master of Science
2016

Advisory Committee:

Professor Siddhartha Das, Chair
Professor Peter W. Chung
Professor Jungho Kim
Professor Amir Riaz

ACKNOWLEDGEMENTS

Foremost, I would like to express my gratitude to both of my research advisors, Professor Siddhartha Das and Professor Peter Chung, for providing me with the opportunity to further my education as a graduate student and research assistant at the University of Maryland under their guidance. I sincerely appreciate all of their tireless and patient support in performing the research reported herein.

I would also like to thank my all of my labmates in the Soft Matter, Interfaces, and Energy Laboratory, especially Ms. Guang Chen and Mr. Shayandev Sinha, for their help and camaraderie over the last two years.

Finally, I am indebted to my family for their support and encouragement of my academic pursuits throughout my life.

TABLE OF CONTENTS

LIST OF TABLES

LIST OF FIGURES

Chapter 1: Introduction

1.1 Background Information

Since it was first isolated in 2004, graphene has generated massive scientific interest due to its unique material properties, which include atomic thinness[1], very high mechanical strength and flexibility[2], large thermal and electrical conductivity[2], and high optical transparency[3]. These properties have led researchers to envision a myriad of potential applications of graphene in fields ranging from biomedical devices to energy storage. The interaction between water and graphene is central to many of these applications such as fabricating graphene membranes for water filtration[4,5] and desalination[4,6,7], devising surfaces for biosensing[8,9], generating electricity[10], and fabricating fuel cells[11] and supercapacitors[12]. Hence, to further the realization of such applications, it is important to understand the behavior of water in contact with graphene surfaces. This behavior is characterized in terms of wetting, which describes the interaction between a liquid drop and a solid (or other immiscible liquid) surface from the time of initial liquid–solid contact to the time that the drop has attained an equilibrium on the solid surface. The initial contact and drop spreading, which are time-dependent processes, are referred to as the wetting dynamics, and the final equilibrium configuration of the drop, which is time invariant, is referred to as the wetting statics.

Wetting is most commonly quantified by two main parameters, the contact angle and the wetted radius, which are defined in Fig. 1a and 1b. For a liquid drop wetting a hydrophilic surface (Fig. 1a), the drop will spread more and wet a large area of the surface, resulting in an equilibrium contact angle less than 90°. On the other hand, for a liquid drop wetting a hydrophobic surface (Fig. 1b), the drop will spread significantly less, resulting

in an equilibrium contact angle greater than 90°. Both superhydrophilicity and superhydrophobicity are found extensively in natural and synthetic systems; superhydrophobicity, in particular, is fundamental for the functioning and survival of several plants[13] and animals[14] and for developing biomimetic water-repelling surfaces for employment in applications such as self-cleaning materials[15], enhanced fluid flow[16], environmental remediation[17], thermal management[18], and energy harnessing[19]. Note that "superhydrophobic" refers to the subset of hydrophobic states having contact angles much greater than 90° – in this work contact angles exceeding ≈120° are classified as superhydrophobic. Superhydrophobicity is a combined consequence of the material properties and geometric configuration of a surface. For example, the interplay of material properties and surface geometry dictates the realization of superhydrophobic states when a water drop attains a Wenzel (*i.e.*, fully-wetted) or Cassie-Baxter (CB) state on a given surface with finite roughness (Fig. 1c and 1d, respectively) – in the Wenzel state, the roughness can increase the contact angle only if the equivalent smooth surface is originally hydrophobic, while in the CB state, the contact angle increases regardless of the original wettability of the equivalent smooth surface[20].

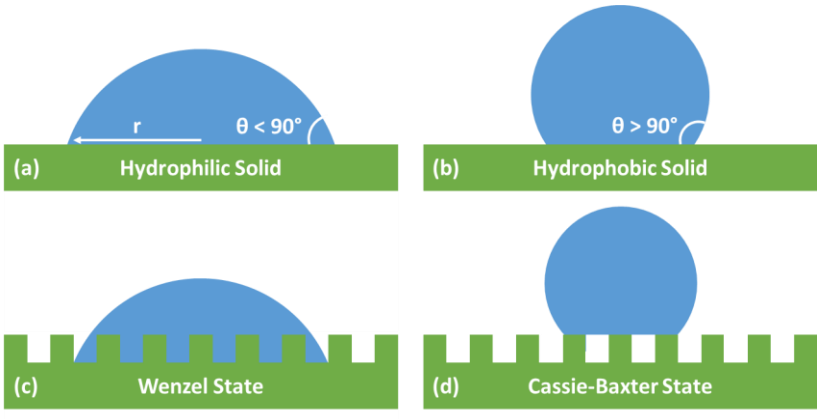

Figure 1: Schematic of (a) wetting on a hydrophilic solid showing the definition of wetted radius r; (b) wetting on a hydrophobic solid; (c) a Wenzel wetting state; (d) a Cassie-Baxter wetting state

1.2 Motivation for the Study of Wetting Dynamics on Smooth Graphene

Extensive research has been performed on the static wetting behavior of smooth graphene-coated substrates, quantified by the equilibrium contact angle of the drop on the graphene surface. While initial studies of the wetting statics of water drops on graphene have yielded contrasting claims of both wetting transparency[21] and opaqueness[22,23], more recent studies indicate that graphene exhibits wetting translucency characteristics[24]. Wetting transparency implies that a graphene coating would have no influence on the contact angle regardless of the nature of the underlying substrate, *i.e.*, the contact angle measured on the graphene-coated substrate would always be identical to that measured on the bare underlying substrate. Wetting opaqueness, of course, implies the opposite – that the contact angle measured on a graphene-coated substrate would always be identical to the contact angle of an unsupported graphene layers, and hence the wettability of the underlying substrate would be completely superseded by the graphene. These disparate observations suggest that graphene may demonstrate more transparency or opaqueness depending on the degree of hydrophilicity or hydrophobicity of the underlying substrate. For example, if the underlying substrate is highly hydrophilic, a monolayer or multi-layer graphene coating will exhibit more wetting transparency with the graphene coating contributing very little to the wetting behavior as compared to the underlying substrate. On the other extreme, if the underlying substrate is strongly hydrophobic, the graphene layers will demonstrate wetting opaqueness, meaning that the graphene layers dominate the wetting behavior and the observed contact angle will be identical to the contact angle on unsupported graphene layers. Therefore, the wettability of the underlying substrate dictates the extent of the apparent hydrophilicity or hydrophobicity of the graphene layers

supported on the substrate, which gives rise to the wetting translucency effect. The fundamental mechanism responsible for such wetting translucency behavior of graphene layers stems from the relative strength of the water–graphene-layer van der Waals (vdW) interactions and water–substrate vdW interactions[24]. For substrates that are highly hydrophilic, water–substrate vdW interactions overcome water–graphene-layer vdW interactions, leading to the wetting transparency of graphene layers; on the other hand, for substrates that are more hydrophobic, water–graphene-layer vdW interactions are stronger, leading to the wetting opaqueness of the graphene layers.

Despite this substantial progress in quantifying the static contact angle of water on graphene, very little research has been done on the wetting dynamics of water on graphene. In other words, there exists no concrete answer to the following question: what are the mechanisms of contacting and spreading of water drops on solids coated with mono- and multi-layer graphene? In Chapter 3, answers are provided to this question by employing molecular dynamics (MD) simulations that quantify, first, the mechanism by which a nanoscopic water drop touches and forms wetting patches on graphene-coated solids and, second, the relationship between the spreading radius (r) and the spreading time (t). Multiple simulations are performed to examine the role of the number of graphene layers as well as the wettability of the underlying solid.

The spreading of the water drop is preceded by the water drop coming into contact with the graphene layers and forming fluctuating patches representing the discrete, molecular nature of the liquid prior to the development of the continuous phase. This patch formation should be identified as an event that signals the transition of the discrete phase molecular regime (associated with the drop just contacting the solid) to the continuous-

phase spreading regime. The first key result presented in Chapter 3 is that such patch formation bears the direct signature of the underlying-solid-induced wettability of the graphene layers, ensuring a faster development of a more uniform patch (*i.e.*, a faster transition from discrete to continuous phase) for graphene supported by a hydrophilic solid as compared to unsupported graphene or graphene supported on a more hydrophobic solid. More importantly, the results demonstrate that the drop spreading on graphene layers, following the patch formation, is characterized by the condition $r \sim t^{1/2}$ for the entire spreading lifetime except for the initial transient period and toward the very end of the spreading process. This $r \sim t^{1/2}$ relationship, establishing that the spreading occurs in the inertial regime, is witnessed regardless of the number of graphene layers or the wettability of the underlying substrate. Remarkably, even a standard LJ liquid nanodrop obeys this same $r \sim t^{1/2}$ relationship during its entire spreading lifetime on standard, non-layered solids[25]. Therefore, in Chapter 3 the following conclusion is made: the spreading dynamics of the wetting of water on graphene, unlike the wetting statics, obey the behavior witnessed in the case of wetting on standard solids.

1.3 Motivation for the Study of Wetting on Nanostructured Graphene

There have been considerable attempts to develop superhydrophobic surfaces that are based on graphene or graphene-derived materials (*i.e.*, graphene oxide) with the intention to marry the benefits of the unique properties of graphene to the advantages intrinsic to superhydrophobic surfaces[26]. Typically, graphene-based superhydrophobic surfaces have been fabricated by two broad approaches. The first approach consists of chemically modifying graphene via, for example, surface functionalization with hydrophobic groups[27,28] or solvent modification[29,30]. The second approach is to impart a

physical deformation on graphene nanosheets (*e.g.*, introducing a crumpling effect)[31–33], which may enforce drops into a superhydrophobic CB state. Despite this progress, there has not been a study that takes advantage of the wetting translucency property of graphene to conceive a possible graphene-based superhydrophobic system. Although wetting on nanostructured materials and the mechanisms by which surface roughness can induce superhydrophobicity (or superhydrophilicity) are fairly well understood[20], there is an absence of studies that probe a condition in which the surface roughness actually affects the original wettability (*i.e.*, the wettability of the equivalent smooth surface) of a given material. Such a situation implies that the wettability on the upper surface of the roughness differs from the case in which there is no roughness, or in other words, there is a wettability gradient across the roughness. As a consequence of its wetting translucency property, this surface-roughness-induced wettability gradient can be achieved for nanostructured graphene (*e.g.*, graphene nanopillars) deposited onto a surface with a different wettability (such as a more hydrophilic substrate).

In Chapter 4, MD simulations are employed to study the wetting of hydrophilic surfaces coated with graphene nanopillars. The wetting translucency effect of graphene ensures a jump in wettability at the nanopillar edge, meaning that the wettability changes depending on whether or not graphene nanopillars are present, as depicted in Fig. 2. It is found that regardless of the wettability of the underlying surface, the presence of graphene nanopillars significantly enhances the contact angle. Therefore, it is shown that graphene nanopillars have the ability to make even a highly hydrophilic surface become superhydrophobic. Most remarkably, the superhydrophobic state that is attained is not a CB state but rather a fully-wetted Wenzel state. Surprisingly, this is effectively a new

Wenzel state in which an increase in roughness (realized as an increase in the nanopillar height) alters the contact angle from the hydrophilic to hydrophobic regime – a behavior not possible in the classical Wenzel state. Finally, it is established that this behavior can be attributed to contact line pinning. In fact, this pinning occurs in a series of pinning-depinning steps during the spreading process. Such pinning occurs due to the jump in wettability at the nanopillar edge, and it is the wetting translucency property of graphene that is responsible for this roughness-dependent wettability jump.

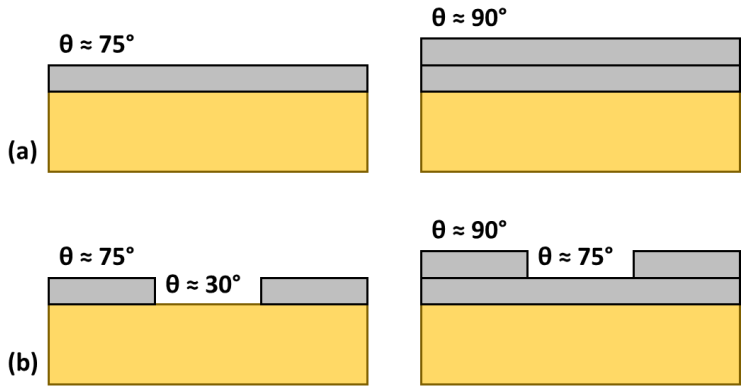

Figure 2: Schematic showing (a) uniform wettability on a hydrophilic substrate coated with smooth monolayer and bilayer graphene; (b) wettability gradient caused the presence of 1-layer graphene nanopillars on a bare hydrophilic substrate and a hydrophilic-substrate-supported graphene monolayer

Chapter 2: Simulation Details and Methodology[1]

2.1 Overview of Molecular Dynamics Simulation

Molecular dynamics simulations are employed to investigate the wetting of water drops on both smooth and nanostructured graphene-coated substrates, and the results and analyses of these simulations are presented in Chapters 3 and 4. In this chapter, the simulation details and methodology are presented. Besides slight changes in the simulations of Chapter 3 to modify the graphene structure for Chapter 4, the details of all simulations reported in Chapters 3 and 4 are nearly identical. All simulations are carried out in the Large-scale Atomic/Molecular Massively Parallel Simulator (LAMMPS)[34] software package. The simulation results are visualized and processed using the Open Visualization Tool (OVITO)[35], and the final analyses are performed in MATLAB.

Fundamentally, a classical MD simulation solves a many-body system of Newton's equations of motion by numerically integrating the trajectories of interacting particles (*i.e.*, atoms or molecules) with respect to time[36]. Of course, the equation of motion for an interacting particle *i* expressed in the Newtonian form is written as[37]

$$m\frac{d^2\boldsymbol{r}_i}{dt^2} = \sum_{j\neq i}^{N} \boldsymbol{f}(r_{ij}), \tag{1}$$

where m is the mass of the particle, $\boldsymbol{r}_i$ is the position of the particle at time t, and $\boldsymbol{f}$ is the force acting on the particle due to the interaction with some other particle j in the N-particle system separated by a distance of r_{ij}. Solving Eq. 1 requires knowledge of $\boldsymbol{f}$, which can of course be expressed as the negative of the gradient of potential energy. This potential

[1] The methodology presented in this chapter has been published as:

Andrews, J., Sinha, S., Chung, P. W., & Das, S. (2016). Wetting Dynamics of a Water Nanodrop on Graphene. *Physical Chemistry Chemical Physics*.

energy is given by empirical potentials, which approximate the forces associated with chemical bonding as well as non-bonded forces arising from vdW or electrostatic interactions[38]. A common empirical potential used to model pairwise vdW interactions is the Lennard-Jones (LJ) model, which has the form[38]

$$U_{ij}^{(LJ)} = 4\varepsilon_{ij}\left[\left(\frac{\sigma_{ij}}{r_{ij}}\right)^{12} - \left(\frac{\sigma_{ij}}{r_{ij}}\right)^{6}\right], \tag{2}$$

where $U_{ij}^{(LJ)}$ is the pairwise interaction energy between atoms *i* and *j*, ε_{ij} gives the depth of the potential well, and σ_{ij} is the separation distance at which the interatomic potential is zero (see Fig. 3). This potential (with parameters as described later in this chapter) is used to model all vdW interactions for the simulations presented in this work.

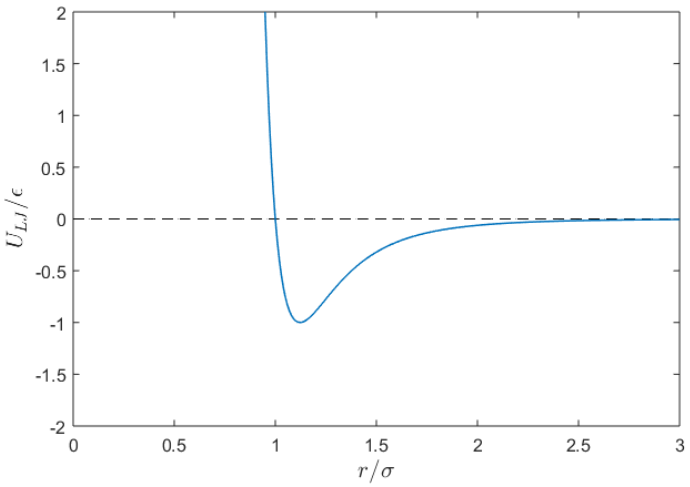

Figure 3: Non-dimensional LJ potential well

Additionally, electrostatic effects are taken into account when modeling water (see Section 2.3) via a Coulombic interaction potential of the form[38]

$$U_{ij}^{(Coul)} = C\frac{q_i q_j}{r_{ij}}, \tag{3}$$

where $U_{ij}^{(Coul)}$ is the electrostatic potential energy, *C* is Coulomb's constant, and q_i and q_j are the charges of particles *i* and *j*, respectively. Note that when applicable, the total

interaction potential between a pair of atoms is simply the superposition of the LJ and Coulombic potentials, that is

$$U_{ij} = U_{ij}^{(LJ)} + U_{ij}^{(Coul)}. \quad (4)$$

2.2 Simulation Size and Geometry

The water drops studied in this work are of a nanoscopic length scale. For drops of such size, curvature-induced line tension at the three phase contact line (TPCL) has a non-negligible contribution to the measured contact angle[21,25,39]. In order to eliminate this system size dependence, a geometry is employed such that the size of the simulation box is much greater than the drop size in the x- and z-dimensions but smaller in the y-dimension (the simulation box is 500 × 20 × 300 Å in x-, y-, and z-dimensions, respectively). Periodic boundary conditions are enforced in all dimensions, resulting in a quasi-2D drop configuration as shown in Fig. 4.

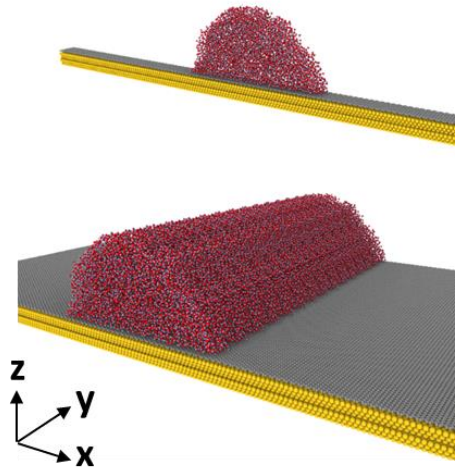

Figure 4: Simulation geometry showing straight TPCL resulting from the quasi-2D drop configuration

In this configuration, the contact line becomes straight, and consequently the effect of the curvature-induced line tension on the contact angle is eliminated. Rafiee *et al.*[21] showed

that for a similar simulation geometry, the system size dependence was eliminated for drops containing at least 2000 water molecules. In the present work, all water drops consist of 4000 water molecules, so the simulations are safely in the domain for which curvature-induced line tension effects can be neglected. Finally, it is worth noting that because wetting can be described as an essentially 2D phenomenon, the results of simulations employing the quasi-2D configuration are expected to hold for real, 3D spherical drops[25].

2.3 Water Model

Water drops are modeled by the extended simple point charge (SPC/E) model[40]. Here, a single water molecule holds the shape of a rigid isosceles triangle where the oxygen and hydrogen atoms are modeled as point masses located at the vertices of the triangle, as shown in Fig. 5.

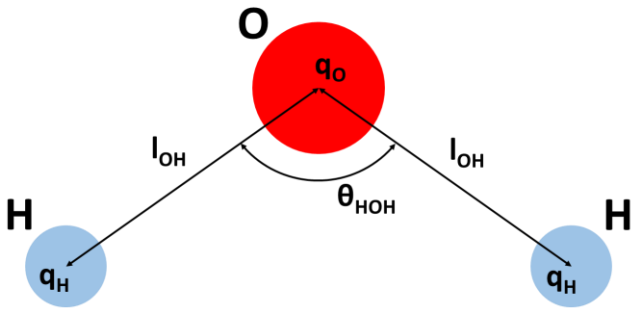

Figure 5: Diagram of SPC/E water model

The O-H bond lengths (l_{OH}) and the H-O-H bond angle (θ_{HOH}) are held fixed using the SHAKE algorithm[41]. As previously noted, water molecules interact via a 12-6 LJ potential as well as Coulombic electrostatic interactions. The LJ potential is cut off at a separation distance (r_c) of 10 Å, and this cutoff radius also serves as the threshold for the transition between short-range and long-range Coulombic interactions. The LJ site is situated on the oxygen atom (LJ parameters ε_{OO} and σ_{OO}), and both the oxygen atom and hydrogen atoms carry partial charges (q_O and $q_{H,}$ respectively). Net electroneutrality is maintained for the

overall molecule. The short-range Coulombic interactions are computed in real space, while the long-range Coulombic interactions are computed in reciprocal space using the particle-particle particle-mesh (PPPM) algorithm[42]. These SPC/E model parameters are summarized in Table 1.

Table 1: Parameters of SPC/E water model

Parameter	Value
l_{OH}	1.0 Å
θ_{HOH}	109.47°
q_O	-0.8476e
q_H	0.4238e
ε_{OO}	0.650 kJ mol^{-1}
σ_{OO}	3.166 Å

2.4 Graphene Coating and Underlying Substrate

In Chapter 3, two cases of wetting of a graphene-coated underlying substrate are considered – one in which the underlying substrate is hydrophobic and one in which it is hydrophilic. The hydrophobic case is taken as unsupported (*i.e.*, free-standing) graphene. For graphene deposited on a more hydrophobic substrate, the underlying substrate would have no influence on the contact angle regardless of the number of graphene layers due to negligible water–substrate interactions as compared to water–graphene interactions. Thus, the absence of an underlying substrate is representative of a hydrophobic underlying substrate. For graphene deposited onto a hydrophilic substrate, however, the underlying substrate can be expected to affect the wetting of the system, so it must be modeled explicitly.

For all simulations reported in both Chapters 3 and 4 containing a hydrophilic substrate, this hydrophilic substrate is modeled as gold where the Au(111) surface is aligned with the graphene lattice[43]. For the gold substrate, the lattice parameter a_{Au} is taken

as the experimental value of 4.08 Å. The graphene lattice parameter a_C is taken as 2.498 Å, which is the experimental value of 2.46 Å stretched by ≈1.5%. This slight stretching of the graphene lattice ensures that the two lattices align as shown in Fig. 6. Rafiee *et al.*[21] employed a similar stretching of the C-C bond to match the graphene lattice to the Cu(111) surface. The interlayer spacing between graphene layers is 3.355 Å, and the spacing between the graphene and gold substrate is taken as 3.31 Å, which is the equilibrium separation distance of a graphene sheet from an Au(111) surface[44].

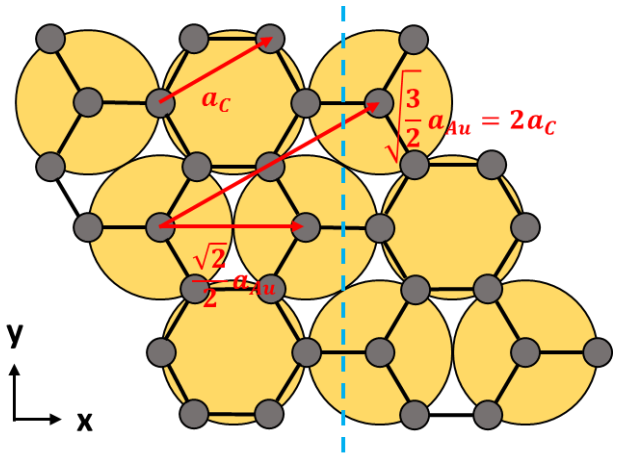

Figure 6: Graphene lattice aligned with Au(111) lattice

The Au and C atoms are fixed at their lattice positions throughout the simulation and only interact with the O atoms of the water molecules via a 12-6 LJ potential. Werder *et al.*[45] have shown that fixing the substrate in this way does not affect the simulated wetting results, though it significantly reduces computational costs. For C–O interactions, the model of Werder *et al.* is adopted, which uses a 12-6 LJ potential (LJ parameters ε_{CO} = 0.392 kJ mol^{-1} and σ_{OO} = 3.19 Å) to model the vdW forces between water molecules and carbon atoms of graphene layers. Experiments by Rafiee *et al.*[21], Shin *et al.*[22], and Wang *et al.*[46] suggest a water drop equilibrium contact angle of ≈90-95° on graphite. Werder *et al.* showed that their model reproduced this experimental value fairly well. The empirical

potential used to model the interaction between water molecules and gold substrate atoms is chosen to produce a hydrophilic substrate having an equilibrium contact angle of ≈25-30°. The model of Merabia *et al.*[47] is adopted, which also employs a 12-6 LJ potential (LJ parameters ε_{AuO} = 2.469 kJ mol^{-1} and σ_{AuO} = 3.6 Å) to model the Au–O interactions and was reported to yield an equilibrium contact angle on the order of 25° for an SPC/E water drop on a gold substrate at 300 K. Again, a 10 Å cutoff distance is applied to all LJ interactions in the system.

Note that these empirical potentials capture all water–substrate interactions via O–substrate LJ interactions and omit any H–substrate interactions. The water–substrate interactions for this system result from dispersion (vdW) forces between water molecules and substrate atoms. Previous simulations of wetting of water on graphene-coated copper substrates[21,23], for which the water–substrate interactions similarly result from dispersion forces only, also employ models in which all water–substrate interaction is accounted for entirely by an O–substrate LJ potential. This justifies the neglect of H–substrate interactions in modeling the water–substrate interactions.

In Chapter 4, systems are investigated for which graphene nanopillars are deposited onto the hydrophilic gold substrate. This structure is achieved by taking smooth graphene layers (with the structure described above) and removing atoms from the lattice at desired locations to create gaps in the bulk graphene, thereby forming nanopillars. Both the nanopillar width and the inter-nanopillar spacing are 13 Å in the x-dimension, and they extend across the entire 20 Å simulation domain in the y-dimension. This 13 Å value is chosen as it is several times greater than the molecular size of water but smaller than the water drop radius ($R \approx 4$ nm). Additionally, because it is very nearly equal to three lattice

spacings, this value produces uniform nanopillars and gaps having a "zig-zag" configuration at all graphene edges (see the blue dashed line in Fig. 6 for an example of a cut yielding the zig-zag arrangement). This zig-zag configuration has been shown experimentally to be the stable arrangement of carbon atoms at the edge of a monolayer graphene sheet[48].

Of course, the graphene-substrate systems described here and implemented in the simulations reported in this work are understood to be idealized models. For example, all materials all chemically pure and free of mechanical inhomogeneities unless intentionally prescribed. Graphene nanopillars are perfectly uniform, and intra-substrate atomic interactions are neglected. Finally, it may not be possible in practice to replicate systems of this sub-nanometer length scale as a consequence of experimental limitations, nor is it realistic to simulate very large macroscale systems due to computational limitations. Nevertheless, these model systems should capture the essential physics of the wetting phenomena as well as allow for a molecular-level analysis not possible given traditional experimental constraints.

Finally, it is worth noting that previous studies describing materials with a nanopillar architecture generally refer to 3D, rod-like structures[49,50]. However, as a consequence of the quasi-2D simulation geometry employed in this work, the simulated nanopillars are only 2D structures. That is, because the drop does not spread in the y-dimension (see Fig. 4), only the x- and z-dimensions are relevant to the drop wetting behavior. Hence, just as the semi-infinite, cylindrical drop is understood as a 2D analog of a 3D, spherical drop, the nanopillars modeled in this work can be considered a 2D analog of the real, 3D nanopillars commonly reported in literature.

2.5 Drop Equilibration and Data Collection

Previous studies that have utilized MD simulations to investigate the wetting of water drops on graphene and graphene-coated substrates have often focused on the wetting statics. In such simulations, the initial configuration of the water drop is not important because the quantities of interest are only measured after the drop has attained an equilibrium state on the substrate. Therefore, in the interest of simplicity, water molecules may be initialized in an ordered, box-like configuration near the substrate, and the system is then evolved forward in time from that state until equilibrium is reached[21]. Here, on the contrary, the wetting dynamics are probed from initial contact to equilibrium; therefore, the entire spreading process must be realistic. To achieve this, the water is first equilibrated far from the substrate starting from an ordered, box-like configuration until a well-formed drop is attained. Note that that radius (R) of the equilibrated drop is approximately 4 nm. This equilibrated drop is then brought near the substrate, after which spreading occurs. This procedure, including both the equilibration and spreading, is shown in Fig. 7 for the case of monolayer graphene deposited onto a hydrophilic substrate.

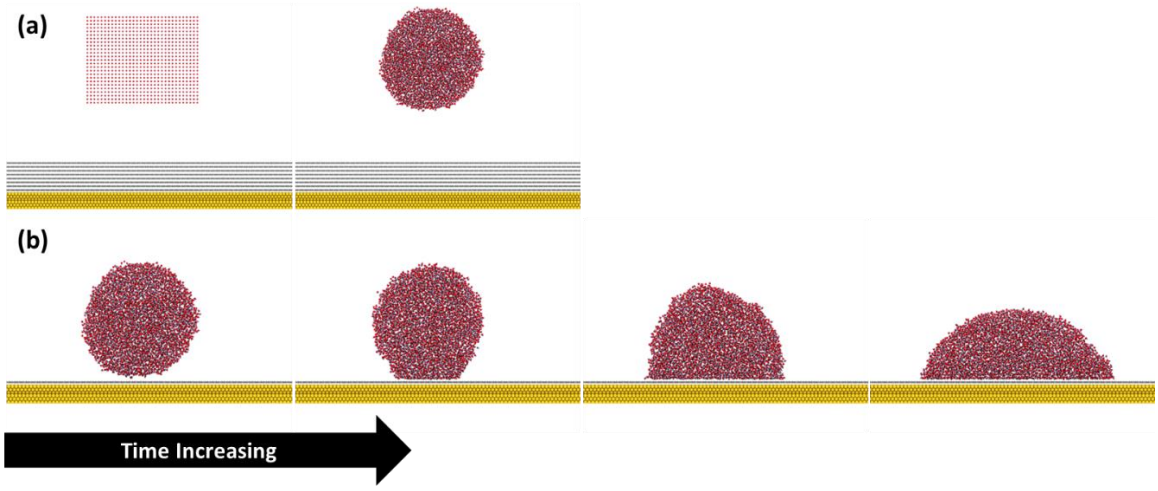

Figure 7: (a) Snapshots of drop equilibration; (b) snapshots of spreading from initial contact to equilibrium for the case of monolayer graphene on hydrophilic substrate

The equilibration phase is carried out in the canonical (NVT) ensemble for a total of 500 ps with a 1 fs timestep. This choice of timestep is deemed appropriate as it yields good long-term energy stability as well as temperature fluctuation within ≈5 K of the 300 K target. The temperature of the water molecules in the starting box-like configuration is initialized at 1 K and then increased to 300 K in 50 K increments. Each intermediate temperature is held constant for 50 ps until reaching 300 K, which is held for 250 ps. Temperature is controlled using the Nosé-Hoover thermostat[51].

Following equilibration, the drop is brought to within ≈3 Å of the substrate. The system then again evolves forward in time with a 1 fs timestep in the NVT ensemble at 300 K. The data collection phases are carried out for 500 or 1000 ps, depending on the time required for a given simulation to reach equilibrium. The Cartesian coordinates of every atom in the simulation are recorded at incremental timesteps to be used in post-processing for the determination of contact angles and wetted radii.

2.6 Post-processing Procedure

The atomic coordinate data is post-processed in MATLAB to calculate quantities of interest such as contact angle and wetted radius, and the procedure is illustrated in Fig. 8 using the example of monolayer graphene on a hydrophilic underlying substrate. First, the coordinate data for all substrate atoms are discarded as they are constrained at their lattice positions throughout the simulations and are not needed to characterize the water drop (Fig. 8a). The 3D coordinate data of water drop atoms are then binned into a 2D grid in the x-z plane (Fig. 8b). To locate the edges of the drop, the bins are systematically checked from the outer grid edges working toward the center; for each row and column, a marker is placed at the center of the first bin for which the number of atoms located within

the bin exceeds a threshold value. These markers then define the profile of the drop (Fig. 8c). To determine the contact angle, a circle is fit to these markers using a least squares regression, and the line tangent to the circle at the point where the circle intersects the upper surface of the substrate is calculated (Fig. 8d). The contact angle is then calculated as the angle through the drop between the line of the upper surface and the tangent line. The wetted radius is calculated as half of the wetted diameter, which is easily measured using the drop profile markers in the vicinity of the substrate.

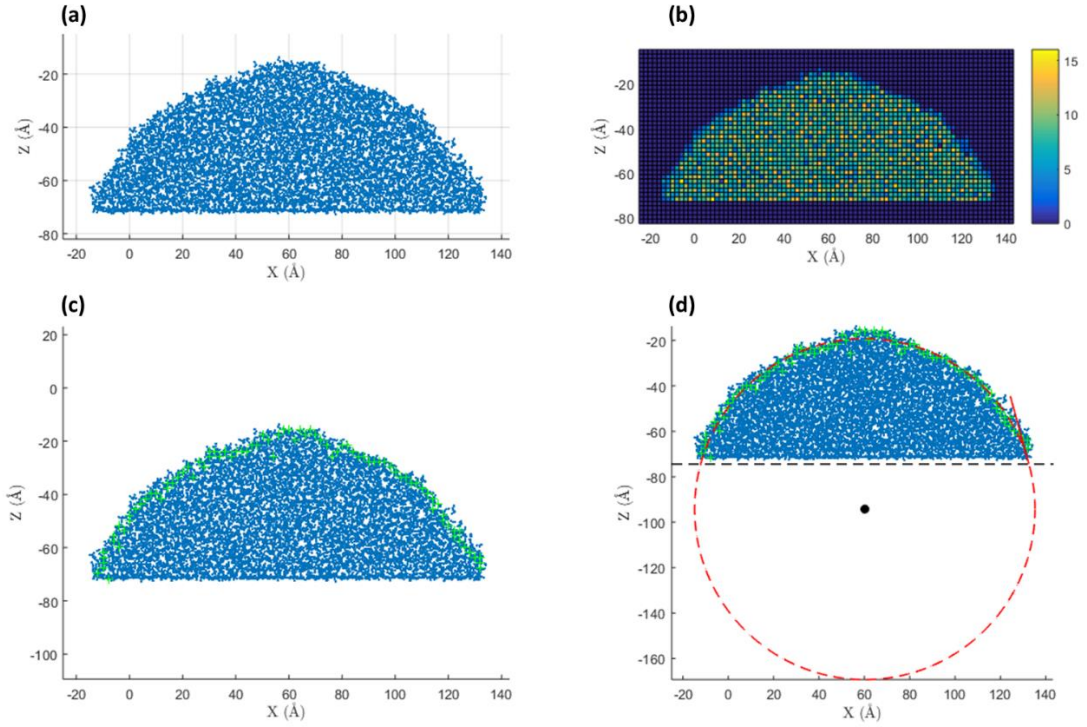

Figure 8: (a) x-z projection of atom coordinate data; (b) binned atom coordinate data; (c) atom coordinate data with markers to define the drop profile; (d) circle fit to drop edge markers and tangent line used to calculate contact angle

Chapter 3: Wetting Dynamics of a Water Nanodrop on Smooth Graphene[2]

3.1 Wetting Statics – Demonstration of the Wetting Translucency of Graphene

Fig. 9 and 10 show the equilibrium contact angles of the water drop on unsupported graphene and graphene supported by a hydrophilic solid, respectively, for varying number (N) of graphene layers. For unsupported graphene with $N = 8$ (see Fig. 9), it is evident that the measured contact angle of ≈90° is in agreement with the experimentally observed contact angle for water on bulk graphite of ≈90-95°[21,22,46]. Furthermore, Fig. 9 reveals that for the case of unsupported graphene, the variation of the number of graphene layers has little effect on the equilibrium contact angle.

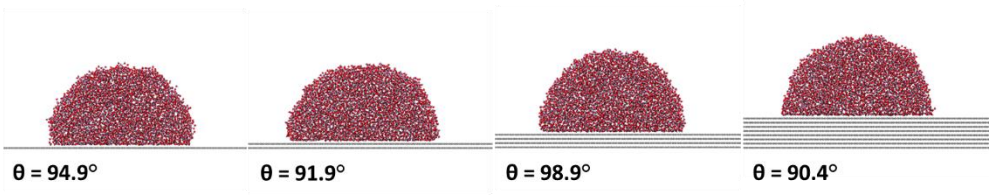

Figure 9: Equilibrium contact angle for unsupported graphene with (from left to right) N = 1, 2, 4, and 8 layers

Shih *et al.*[24] first introduced the concept of wetting translucency by showing that an increase in the number of graphene layers leads to a progressive (though not significant) decrease in the contact angle. They argued that had graphene layers been wetting opaque or wetting transparent, the water drop contact angle would be identical regardless of the number of layers. On the other hand, Rafiee *et al.*[21] established this wetting translucency nature (although they denoted it as "wetting transparency of graphene") by demonstrating

[2]The results presented in this chapter have been published as:

Andrews, J., Sinha, S., Chung, P. W., & Das, S. (2016). Wetting Dynamics of a Water Nanodrop on Graphene. *Physical Chemistry Chemical Physics*.

through experiments that the water drop contact angle on a single layer of graphene supported by an underlying hydrophilic solid like glass, on which the contact angle of water is ≈20°, can be as low as ≈48°. However, the contact angle on a single layer of graphene supported by copper, on which the contact angle of water is ≈85.9°, is ≈86.2°. This attainment of a contact angle (≈48°) on a single layer of graphene on glass that is intermediate to the contact angle on bare glass (≈20°) and the contact angle (≈90°) on a single layer of unsupported graphene or a single layer of graphene supported on a less wetting solid (*e.g.*, on copper) is the perfect example of the wetting translucency nature of graphene. Given the fact that Rafiee *et al.* provided both simulations and experiments to discuss their results, those results are used as a benchmark to validate the accuracy of the simulation results presented here. They identified (both through experiments and MD simulations) that the contact angle of water on graphite (6-8 layers of graphene) is ≈90-94° regardless of the nature of the underlying substrate. This contrasts with the findings of Shih *et al.*, who showed a progressive decrease in the contact angle with an increase in the number of unsupported graphene layers and witnessed a value of $\theta = 78°$ for $N = 3$. Hence, for graphite (N = 6-8), the contact angle would be much smaller than the experimentally determined value. Therefore, little emphasis is placed on why the water drop contact angles, unlike the predictions of Shih *et al.*, do not show appreciable variation with change in the number of layers of unsupported graphene, and the validation of the simulations is established by the fact that they reproduce the experimentally observed value of the water contact angle on graphite. Further, the contact angles on different numbers of graphene layers supported by copper (recall that bare copper has a water contact angle of ≈85.9°) show negligible variation as a function of the number of graphene layers[21]. Given the fact

that this wetting translucency is dictated by vdW forces of interaction, which correspond to the value of the contact angle, the presence of copper is nearly equivalent to the presence of graphene since the contact angles on both copper and unsupported graphene are very similar. Consequently, the finding that the contact angle on unsupported graphene layers shows negligible variation as a function of the number of layers can be justified from the experimental observation of nearly non-varying contact angle on different numbers of graphene layers supported by copper.

This difference between the results of Rafiee *et al.* (and this study) and Shih *et al.* possibly stem from consideration of a finite size drop by Shih *et al.* as compared to an infinite drop (achieved in the manner described in section 2.2) by Rafiee *et al.* For a finite size nanodrop, a drop-size-dependent line tension effect is introduced, enforcing an expression of contact angle as[39]

$$\cos(\theta) = \cos(\theta_\infty) - \frac{\tau}{\gamma r}, \tag{5}$$

where τ is the free-energy contribution due to line tension, γ is the water surface tension, r is the radius of the circular contact line, θ is the equilibrium contact angle observed from the nanodrop snapshot through MD simulation, and θ_∞ is the contact angle for an infinitely large drop in which there is no line tension effect. Consequently, the result depends on estimation of τ and its non-trivial dependence on the number of graphene layers – a negative value of τ, as reported by Shih *et al.*, apparently explains a reduced value of the contact angle. On the contrary, the simulations of Rafiee *et al.* and this work employ a semi-infinite (quasi-2D) drop, thereby removing this line tension dependence of the contact angle.

Fig. 10 shows the contact angle of a water drop supported on a hydrophilic surface. Note that the equilibrium contact angle of the water drop on the bare hydrophilic surface

is $\theta_{eq,bare} \approx 30°$, *i.e.*, the surface is similar to a gold surface[47]. First, the case of a water drop on a single layer of graphene on this hydrophilic surface is considered. The observed contact angle is ≈75°, which is a significant reduction of the contact angle as compared to that on unsupported monolayer graphene. This clearly demonstrates the wetting translucency nature of graphene, similar to the wetting translucency exhibited by the attainment of an intermediate contact angle when water is placed on a single layer of graphene supported by glass[21]. Wetting transparency would have meant that the observed contact angle corresponded to the bare hydrophilic surface (*i.e.*, $\theta \approx 30°$), while wetting opaqueness would have meant that the observed contact angle corresponded to a single layer of unsupported graphene (*i.e.*, $\theta \approx 90°$). An increase in the number of graphene layers for this case of supported graphene, of course, leads to a contact angle that is similar to that for unsupported graphene. This can be justified by the reduction in the influence of the water–substrate vdW interactions, which causes the deviation in the contact angle as compared to the unsupported graphene case. Such a behavior is attributed to the greater distance between the water drop and the substrate as well as the greater contribution of water–graphene vdW interactions as compared to water–hydrophilic-substrate vdW interactions for a larger number of graphene layers.

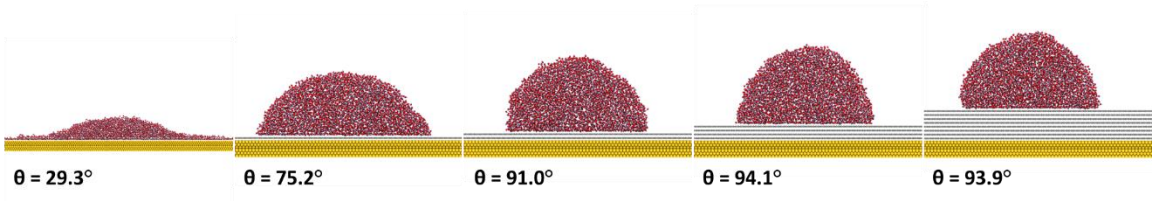

Figure 10: Equilibrium contact angle for graphene supported by a hydrophilic substrate with (from left to right) N = 0, 1, 2, 4, and 8 layers

3.2 Initial Drop Contact – Patch Formation

Fig. 11-16 quantify the dynamics of the water nanodrop as it establishes contact with the graphene layers. This contact leads to the formation of patches (or clusters) of water molecules prior to the attainment of a uniform distribution of water molecules near the substrate surface (see Fig. 12-15). These patches, signifying the early stages of the interaction between the water drop and graphene layers, represent the case where one encounters the discrete, molecular nature of the liquid that is yet to form the continuous phase. In other words, these patches signify the stage of the wetting process during which the drop transitions from a discontinuous molecular phase (at the initiation of contact of the drop with graphene) to the continuum spreading phase. To probe this patch formation and transition, the water molecules in a defined region very near to the upper surface are considered. This region, which is depicted by the green box in Fig. 11, has a width of 50 Å (x-dimension) centered at the point where the drop makes first contact with the substrate, depth of 20 Å (y-dimension), and height of 5 Å (z-dimension) from the top of the substrate.

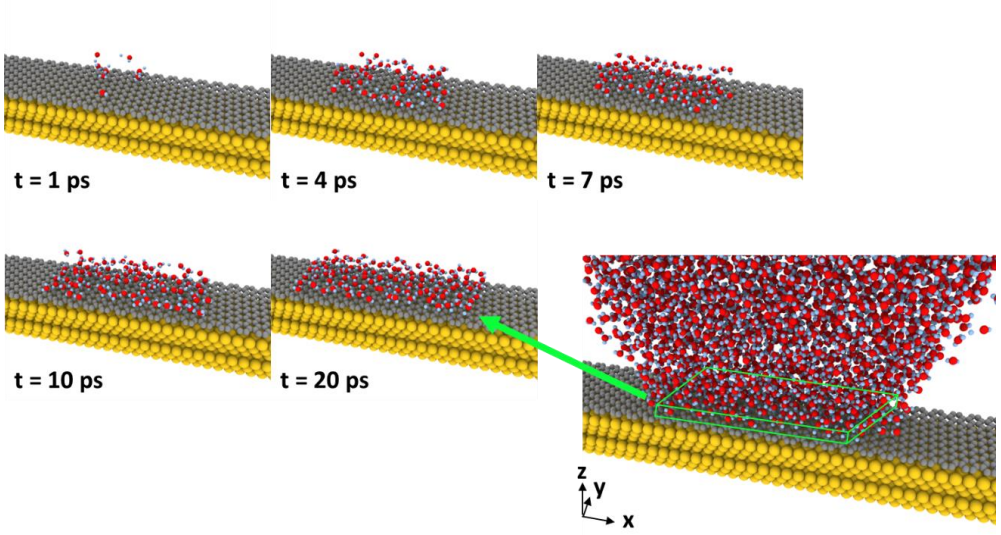

Figure 11: 3D visualization of drop–substrate initial contact and patch formation, showing in particular the 50 × 20 × 5 Å region (represented by the green box) corresponding to the patch formation analysis

The patch formation is shown as 3D visualizations as well as 2D x-y projections for the cases of unsupported monolayer graphene (Fig. 12), unsupported 4-layer graphene (Fig. 13), monolayer graphene on hydrophilic underlying substrate (Fig. 14), and 4-layer graphene on hydrophilic underlying substrate (Fig. 15). There is not much discernable difference between the patch formation events for a water drop contacting different numbers of unsupported graphene layers as there is insignificant difference in the water equilibrium contact angle, and hence water–graphene interaction energy, for different numbers of unsupported graphene layers (see Fig. 9). However, the issue becomes non-trivial for graphene supported on the hydrophilic solid. Here, for a water nanodrop on a single layer of graphene, the patch formation is significantly enhanced. In other words, a more uniform patch develops over a much smaller time, indicating a progress toward the attainment of the continuous phase over a much smaller time.

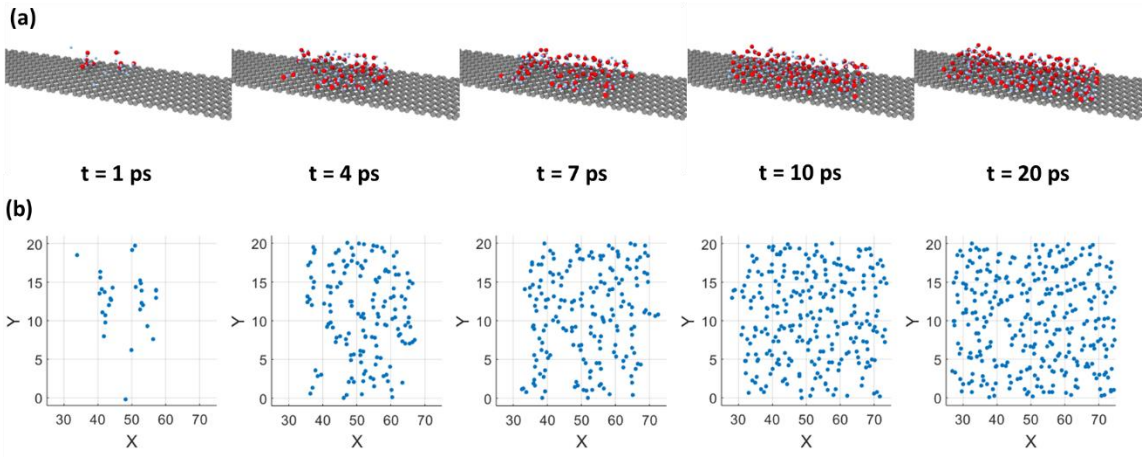

Figure 12: (a) 3D visualization of patch formation on unsupported monolayer graphene for t = 1, 4, 7, 10, and 20 ps; (b) x-y projections (axes in units of Å) of the visualizations shown in (a)

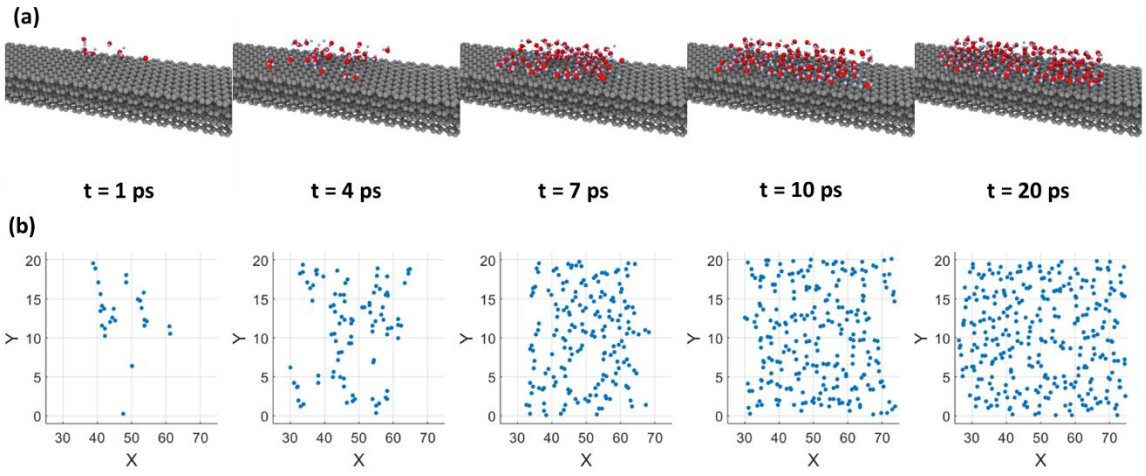

Figure 13: (a) 3D visualization of patch formation on unsupported 4-layer graphene for t = 1, 4, 7, 10, and 20 ps; (b) x-y projections (axes in units of Å) of the visualizations shown in (a)

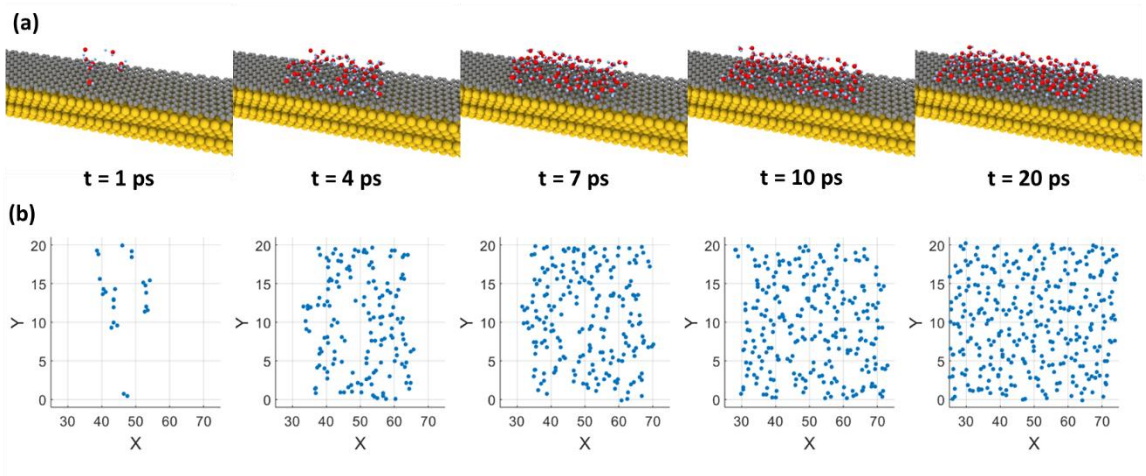

Figure 14: (a) 3D visualization of patch formation on monolayer graphene supported on hydrophilic substrate for t = 1, 4, 7, 10, and 20 ps; (b) x-y projections (axes in units of Å) of the visualizations shown in (a)

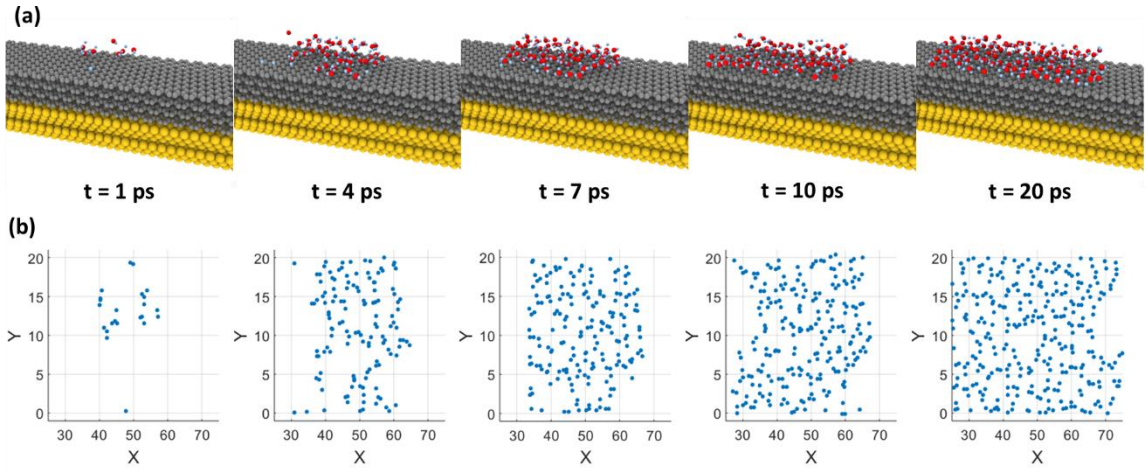

Figure 15: (a) 3D visualization of patch formation on 4-layer graphene supported on hydrophilic substrate for t = 1, 4, 7, 10, and 20 ps; (b) x-y projections (axes in units of Å) of the visualizations shown in (a)

Qualitatively, this can be seen by comparing the patch formation at t = 7 and 10 ps for N = 1 and N = 4 in Fig. 14 and Fig. 15, respectively. Such a behavior can be directly attributed to the much smaller equilibrium contact angle for this case of monolayer graphene on a hydrophilic solid (see Fig. 10), which corresponds to more favorable water–substrate interaction energy and eventually leads to enhanced patch formation.

The patch formation is quantified in terms of the temporal variation of the surface number density of atoms in the patch (see Fig. 16). As expected, there is no difference in the number density between cases N = 1, 2, 4, and 8 for unsupported graphene (Fig. 16a), while the case of N = 1 is notably distinct from cases N = 2, 4, and 8 for graphene on a hydrophilic substrate (Fig. 16b). It is clearly seen that for hydrophilic-substrate-supported monolayer graphene, the number density is substantially greater at a given time, indicating the transition from the molecular phase to the continuum phase over a smaller time. Of course, all plots eventually saturate over longer time, which indicates the attainment of the continuous phase and the onset of the spreading process. Such an inference can be justified by the fact that once the spreading starts, the water molecules access other locations away

from the zone of interest (*i.e.*, the region where the drop first touched the surface and patch formation began), with the number of molecules within the zone of interest that is already wetted ceasing to change. Therefore, through a careful analysis of the patch formation process, it is possible to quantify the time when the liquid drop attains a continuous phase, which in turn signals the onset of the spreading process.

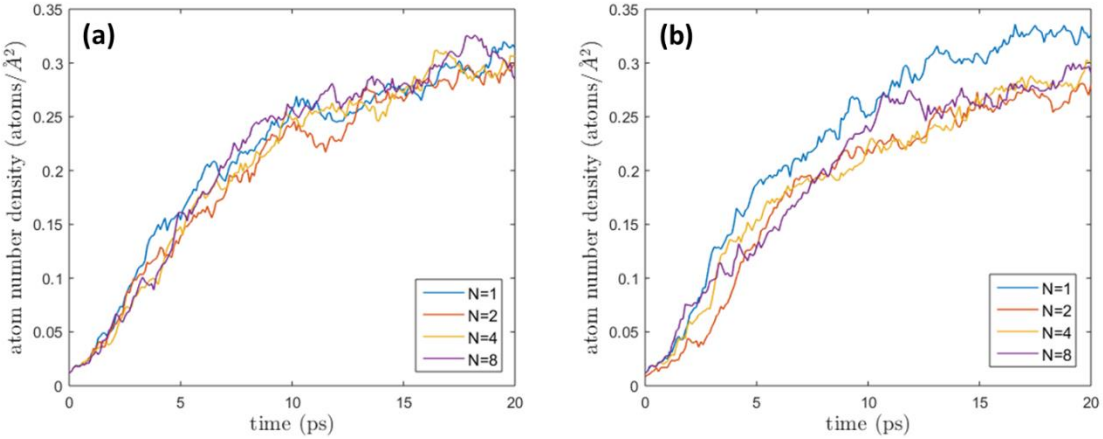

Figure 16: Number density of atoms located within a 50 × 20 × 5 Å region on the surface of the substrate (see Fig. 11) immediately after the drop is brought near to the substrate for (a) unsupported graphene with N = 1, 2, 4, and 8 layers and (b) graphene on a hydrophilic underlying substrate with N = 1, 2, 4, and 8 graphene layers

3.3 Spreading Dynamics

After the water drop has established contact with the graphene layers, it starts to spread. This spreading is quantified in terms of the variation of the spreading radius (r) (see Fig. 1a for the definition of r) as a function of the spreading time (t). Fig. 17a and 17b depict the r *vs.* t variation (r has been made dimensionless by the initial drop radius R and t with the capillary time scale τ_c) for unsupported graphene and graphene supported on a hydrophilic substrate, respectively. The capillary time scale is written as

$$\tau_c = \sqrt{\frac{\rho R^3}{\gamma}}, \tag{8}$$

where ρ is the density and γ the surface tension of water. Regardless of the number of graphene layers or the nature of the underlying substrate, $r \sim t^{1/2}$ is observed consistently for the entire spreading time except for the initial transience and at the very end when the drop stops spreading and hence r no longer changes with time. This is the central result of this chapter on the wetting dynamics on smooth graphene and graphene-coated substrates.

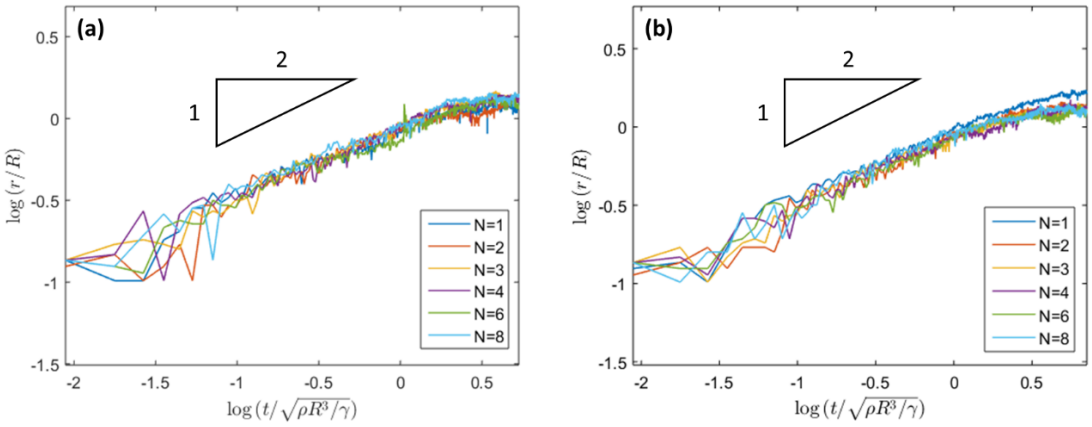

Figure 17: Non-dimensional r vs. t variation for (a) unsupported N-layer graphene; (b) N-layer graphene supported by a hydrophilic substrate

This particular $r \sim t^{1/2}$ signals that the entire (except for the initial transience and at the very end) nanodrop spreading process on graphene layers, irrespective of the number of layers or the nature of the underlying substrate, occurs in the inertial regime. This is exactly identical to the spreading of a standard LJ nanodrop on standard, non-layered solids of different wettabilities[25]. Therefore, these simulations establish that unlike the wetting statics of graphene, which demonstrates the unique phenomenon of wetting translucency, the wetting dynamics obey the inertial regime (characterized by $r \sim t^{1/2}$) as witnessed for standard, non-layered solids.

Of course, the inertial regime is interpreted as the regime for which the spreading occurs by the balance of inertial pressure inside the drop and capillary pressure associated with the drop curvature. The inertial pressure is given by

$$p_{inertial} \sim \rho \left(\frac{dr}{dt}\right)^2, \tag{9}$$

and the capillary pressure is given by

$$p_{cap} \sim \frac{\gamma R}{r^2}. \tag{10}$$

Consequently, balancing Eq. 9 and 10 yields

$$\begin{aligned} p_{inertial} &\sim p_{cap} \\ \rho \left(\frac{dr}{dt}\right)^2 &\sim \frac{\gamma R}{r^2} \\ r dr &\sim \sqrt{\frac{\gamma R}{\rho}}\, dt \\ r &\sim \left(\frac{\gamma R}{\rho}\right)^{1/4} t^{1/2} \\ \frac{r}{R} &\sim \left[t \Big/ \left(\frac{\rho R^3}{\gamma}\right)^{1/2}\right]^{1/2}, \end{aligned} \tag{11}$$

which shows that $r \sim t^{1/2}$ is recovered in the inertial regime, as seen for the simulations in Fig. 17.

Fig. 18 and 19 probe the spreading dynamics in terms of the energy variation. These figures show the temporal variation of the potential energy of the system for water drop spreading on unsupported graphene and graphene supported by a hydrophilic substrate, respectively. The plots are smoothed using a 5-point moving average for clarity. Note that this is the potential energy of the entire system scaled by the number of water molecules in the drop, which is 4000 for all simulations. The potential energy of the system is calculated as the sum of all pairwise interaction energies (*i.e.*, water–water LJ interaction, water–

substrate LJ interaction, and water–water Coulombic interaction). Of course, there is a contribution from the kinetic energy to the overall system energy as well, but because the simulations are carried out at constant temperature, the kinetic energy simply fluctuates about a contestant value without any remarkable trend in time. These results connect the information on water–carbon and water–gold molecular level interactions to the spreading dynamics. First, at $t = 0$ (i.e., prior to the start of spreading), the overall potential energy of the system is ≈-45.5 kJ mol^{-1}, which is consistent with the potential energy of bulk water in the SPC/E model (≈-46 kJ mol^{-1})[52]. This signifies the stage at which the drop initiates spreading from an initial spherical shape. Second, it is seen that for drops on both unsupported graphene and graphene supported on a hydrophilic underlying substrate, the drop spreading is characterized by a lowering (*i.e.*, increase in the negative magnitude) of the overall energy, establishing the spontaneity of the spreading process. Eventually, this decrease in energy stops, indicating that the spreading process has ceased. Finally, from the eventual value at which the potential energy saturates, it is possible to make a qualitative inference about the extent of spreading, or equivalently, the extent of the wettability. For example, for a water drop wetting a bare hydrophilic surface, the final value of the energy is substantially smaller as compared to those for different numbers of graphene layers supported on the hydrophilic surface (see Fig. 19a), commensurate with a much smaller contact angle for water on the bare hydrophilic surface. Of course, for monolayer graphene on a hydrophilic substrate, the water contact angle is lesser than for multiple layers of graphene ($N = 2$ and 4), and accordingly, this saturation energy value is smaller for $N = 1$ as compared to $N = 2$ and 4 (see Fig. 19b). Such overall reduced energy

(or equivalently, more hydrophilic equilibrium state) is directly commensurate with the much larger value of ε_{AuO} (2.469 kJ mol^{-1}) as compared to ε_{CO} (0.392 kJ mol^{-1}).

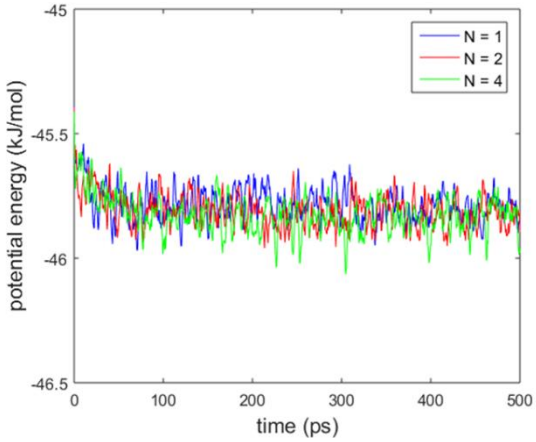

Figure 18: potential energy vs. time for N-layer unsupported graphene

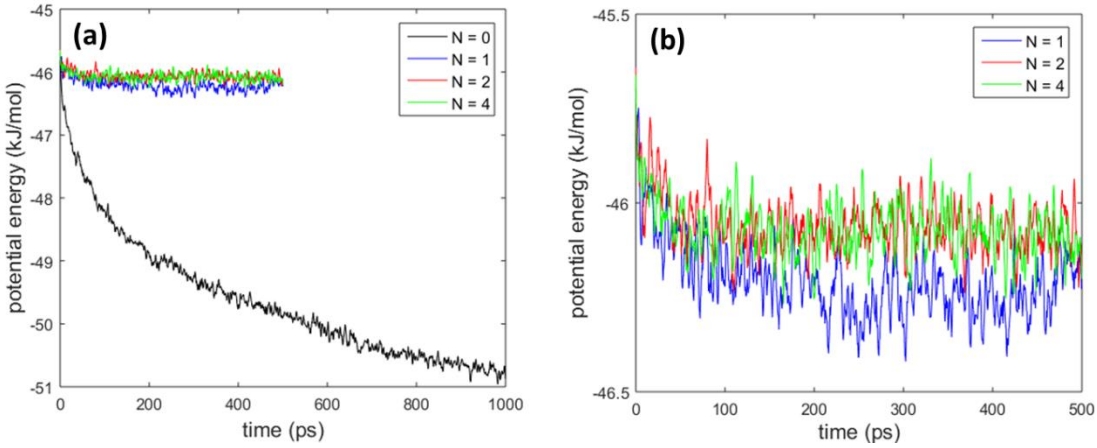

Figure 19: (a) potential energy vs. time for N-layer graphene supported by a hydrophilic substrate; (b) view of the same data as (a) without N = 0 for clarity

3.4 Discussion of Spreading Regime

The present study, as well as the study on nanodrop spreading by Winkels *et al.*[25], establishes that the spreading of a nanodrop for both graphene and standard, non-layered solids occurs entirely in the inertial regime except for the initial transience and the saturation behavior at the very end of the spreading. Being in the inertial regime implies that there is no role of the liquid viscosity in the spreading of nanodrops. Such strictly

inertial spreading is justified by both Winkels *et al.* and this study by demonstrating the $r \sim t^{1/2}$ spreading behavior of the drops, confirming that the spreading occurs by the balance of the inertial and capillary forces with the capillary time scale being the relevant time scale for the process.

It is worth considering, however, how nanodrop spreading in the viscous regime differs from spreading in the inertial regime. It is vital to understand this difference in order to be sure that the majority of the spreading occurs in the inertial (or inviscid) regime. If the spreading had occurred in the viscous regime, then it would be driven by the balance of the viscous pressure (or viscous stress) and the capillary pressure where the capillary pressure drives the spreading and the viscous stress resists it. Given the viscous pressure,

$$p_{viscous} \sim \eta \frac{(dr/dt)}{r}, \tag{12}$$

where η is the dynamic (shear) viscosity of the liquid, the balance of viscous and capillary pressures for viscous spreading yields:

$$\begin{gathered} p_{viscous} \sim p_{cap} \\ \eta \frac{(dr/dt)}{r} \sim \frac{\gamma R}{r^2} \\ r dr \sim \frac{\gamma R}{\eta} dt \\ r \sim \left(\frac{\gamma R}{\eta}\right)^{1/2} t^{1/2} \\ Oh \frac{r}{R} \sim \left[\frac{t}{{\tau_v}^{1/2}}\right]^{1/2}. \end{gathered} \tag{13}$$

Here, τ_v is the viscous time scale, given by

$$\tau_v = \frac{\rho R^2}{\eta}, \tag{14}$$

and Oh is the Ohnesorge number, given by

$$Oh = \frac{\tau_c}{\tau_v} = \frac{\eta}{\sqrt{\rho R \gamma}}, \quad (15)$$

which provides the ratio of inertial to viscous time scales[53]. From Eq. 13, it is evident that nanodrop spreading in the purely viscous regime will also yield $r \sim t^{1/2}$ dynamics; the only exception is that unlike spreading in the inertial regime, here the relevant time scale is τ_v rather than τ_c. This, therefore, establishes that $r \sim t^{1/2}$ is not a unique signature for the nanodrop spreading in the inertial regime, and the spreading may actually occur in the viscous regime. Hence, in order to distinguish in which regime (inertial or viscous or mixed) the spreading occurs, it is worthwhile to probe the time scales of these regimes. Using the values of ρ = 1000 kg m^{-3} and γ = 70 mN m^{-1} for water with $R \approx 4$ nm in Eq. 8 yields $\tau_c \approx 30$ ps for spreading in the inertial regime. For spreading in the viscous regime, the time scale is calculated from Eq. 14 as $\tau_v \approx 16$ ps taking $\eta = 0.001$ Pa s. Therefore, it is found not only in terms of the scaling behavior (*i.e.*, $r \sim t^{1/2}$) but also in terms of the overall time scale for the process that inertial and viscous spreading regimes for the nanodrop are very much similar. Such a finding may cast doubt on the observation that the nanodrop spreading occurs entirely in the inertial regime. However, for nanoscopic liquid–solid interfaces, there is inevitably a drastic reduction in the viscosity by at least four to five orders on account of possible layering of water molecules normal to the water–graphene interface[54–57]. This reduction is also quantified in terms of the presence of a very large slip length[58]. Accordingly, the viscous time scale will undergo a four to five order of magnitude enhancement, thereby making the viscous time scale of the order of several nanoseconds. Thus, now the capillary time scale becomes smaller than the viscous time scale by several orders – MD simulations by Winkels *et al.*[25] as well as those presented here demonstrate

that the spreading occurs only on the order of picoseconds, and therefore the spreading must take place in the inertial regime and not in the viscous regime.

Chapter 4: Wetting of a Water Nanodrop on Nanostructured Graphene

4.1 Wetting Statics – Nanostructure-induced Superhydrophobicity of Graphene

Fig. 20 shows the equilibrium drop profiles and contact angles for the wetting of nanopillars consisting of *n* layers of graphene supported by a bare hydrophilic (gold) substrate. For *n* = 1-3, the drop attains a fully-wetted Wenzel state, while for *n* = 4, the CB state is attained.

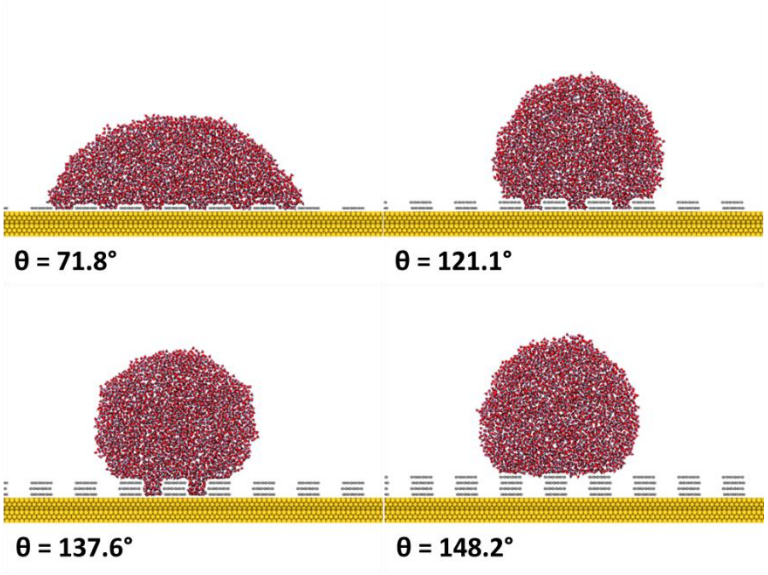

Figure 20: Equilibrium drop configuration with contact angle for the wetting of n-layer graphene nanopillars on a bare hydrophilic substrate with n = 1, 2, 3, and 4

Remarkably, there is a substantial difference in the contact angle values witnessed from the MD simulations (θ_{MD}) and those predicted from analytical theory (θ_W, see Appendix A for the derivation of θ_W). The observed and theoretical values are summarized in Table 2.

Table 2: Observed (through MD simulation) and predicted contact angles for wetting on n-layer graphene nanopillars on a bare gold substrate

Number of Layers in the Graphene Nanopillars (*n*)	Observed Contact Angle (θ_{MD})	Predicted Contact Angle (θ_W or θ_{CB})
1	71.8°	50.1°
2	121.1°	58.6°
3	137.6°	58.5°
4	148.2°	122.4°

The MD-simulated contact angle values are in the superhydrophobic range for n = 2-4. Graphene is known to exhibit such a degree of hydrophobicity only when it has been chemically modified or mechanically crumpled[31–33], which enforces the drop to attain a CB state. On the contrary, the MD simulations yield such contact angles even when the drop is in the fully-wetted Wenzel state. Furthermore, these Wenzel states are actually new Wenzel states that are hitherto unreported in literature. This stems from the fact that with an increase in roughness (from n = 1 to n = 3), there a progressive increase in the contact angle and more importantly, a transition from hydrophilic ($\theta < 90°$) to hydrophobic ($\theta > 90°$) wetting regime. Classical Wenzel states are characterized by the fact that an increase in roughness augments the intrinsic wetting property of the surface. In other words, hydrophilic becomes more hydrophilic and hydrophobic becomes more hydrophobic, but there is never a transition from a hydrophilic to hydrophobic state[20]. However, such a transition is witnessed here with an increase in roughness; hence, it can be categorized as a new Wenzel state. Additionally, a greater contact angle as compared to that predicted by theory is observed even for the case of wetting in the CB state (n = 4).

In Fig. 21, the equilibrium drop profiles and corresponding equilibrium contact angle values are shown for the wetting of n-layer graphene nanopillars on monolayer graphene supported by a hydrophilic (gold) substrate. Note that this graphene monolayer supported by the gold substrate is a continuous, smooth (i.e., non-perforated) layer.

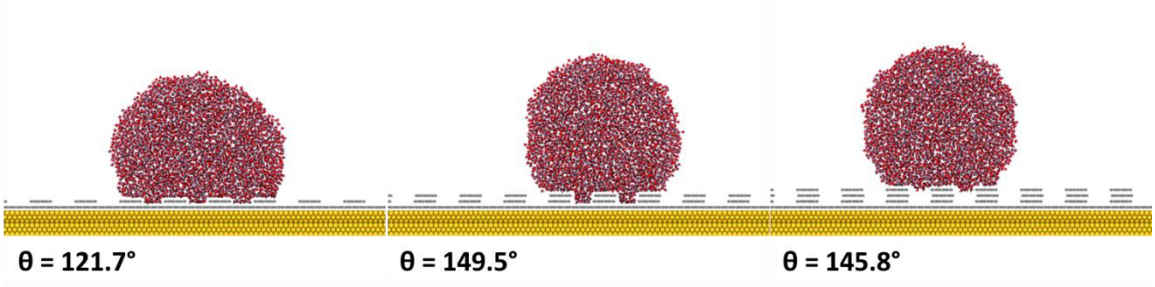

Figure 21: Equilibrium drop configuration with contact angle for the wetting of n-layer graphene nanopillars on monolayer graphene supported by a hydrophilic substrate with n = 1, 2, and 3

Again, the simulation results yield contact angles that are significantly greater than those predicted by analytical theory, as shown in Table 3.

Table 3: Observed (through MD simulation) and predicted contact angles for wetting on n-layer graphene nanopillars on gold-supported monolayer graphene

Number of Layers in the Graphene Nanopillars (n)	Observed Contact Angle (θ_{MD})	Predicted Contact Angle (θ_W or θ_{CB})
1	121.7°	82.3°
2	149.5°	82.2°
3	145.8°	122.4°

Here, the drop is in the fully-wetted Wenzel state for n = 1 and 2 while it attains the CB state for n = 3. Recall that the equilibrium contact angle for water on monolayer graphene supported by this hydrophilic gold substrate is ≈75° (see Section 3.1). Therefore, this extremely large, superhydrophobic contact angle in the Wenzel state (n = 1 and 2) marks a transition of Wenzel contact angle from the hydrophilic to hydrophobic regime, signifying that here too this new Wenzel state is encountered. In fact, the Wenzel contact angle for n = 2 is comparable to CB contact angle observed for n = 3.

Fig. 20 and 21 establish that graphene nanopillars can induce superhydrophobicity in originally hydrophilic surfaces such as bare gold, where the native water contact angle is ≈30°, or monolayer graphene supported by gold, where the native water contact angle is ≈75°. Furthermore, the contact angle values observed from the MD simulations are

significantly greater than those predicted by analytical theory. This nanostructure-induced superhydrophobic behavior can be explained by pinning of the contact line, which depends on the interplay of the surface roughness (introduced by the presence of the nanopillars) and graphene's wetting translucency property.

4.2 Origin of Superhydrophobic Wenzel-like States – Contact Line Pinning

4.2.1 1-layer Graphene Nanopillars on Bare Hydrophilic Substrate

Fig. 22 shows several MD simulation snapshots illustrating the contact line dynamics for spreading of the water nanodrop on 1-layer graphene nanopillars on a bare hydrophilic substrate.

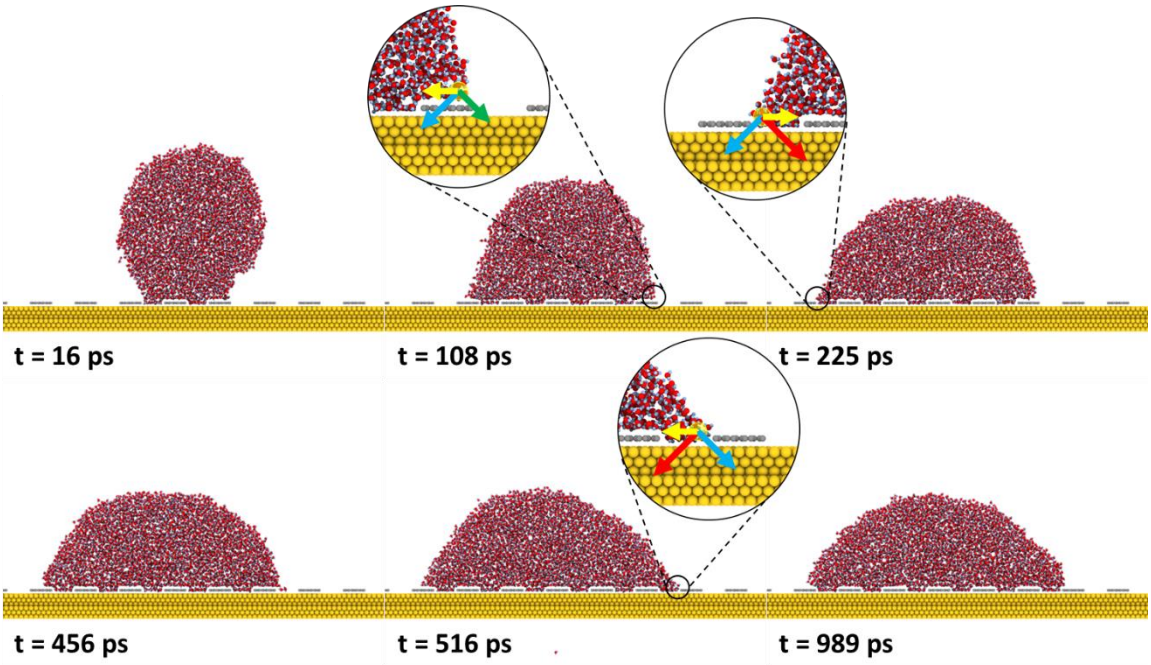

Figure 22: Snapshots of drop spreading for 1-layer graphene nanopillars on a bare hydrophilic substrate

The snapshot at t = 16 ps shows the onset of the spreading process. Studying the forces on the contact line during this spreading process is central to elucidating how pinning occurs and arrests the contact line movement. Of course, a force should be understood to act on a mass and not a line; therefore, by "force on the contact line," force on a mass of liquid in

the vicinity of the contact line is actually implied[59], as shown in Fig. 23. This mass element will be subject to four different forces. The forces F_{LV} and F_{SL} are the forces at the liquid–vapor and solid–liquid interfaces (and not the three phase contact line). As explained by Marchand *et al.*[59], these two forces are primarily associated with the anisotropy caused by the introduction of the second phase (solid or gas) in the bulk liquid. For a drop on a homogeneous solid, the net horizontal attractive force on the contact line from the solid is zero. Therefore, it is the net horizontal force resulting from the difference of F_{LV} and F_{SL} that causes the spreading. However, the nature of the attractive force from the solid changes the moment there is a surface inhomogeneity, as for example in the present case. In the present study, when near to the nanopillar edges, the contact line is subject to unequal attractive forces from the graphene nanopillar and the underlying hydrophilic substrate ($F_{a,Gr}$ and $F_{a,Go}$ in Fig. 23, respectively). For the drop configuration in which this resultant horizontal force becomes equal and opposite to the horizontal spreading forces resulting from F_{LV} and F_{SL}, the contact line becomes pinned.

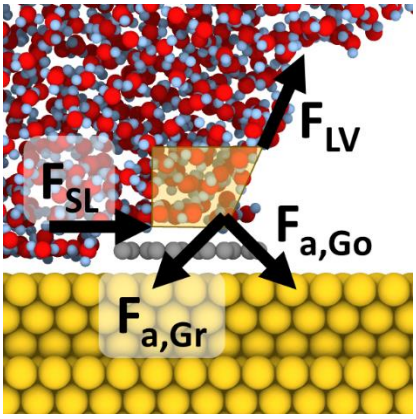

Figure 23: Complete force diagram acting on a finite mass of water in the vicinity of the contact line showing the forces responsible for promoting/retarding spreading (snapshot shown is for 1-layer graphene nanopillars on bare gold at t = 16 ps, but the force diagram is relevant for all times and nanopillar/substrate configurations)

Returning to Fig. 22, at t = 108 ps the right contact line becomes pinned as a result of a pinning force that balances the spreading force, and hence the contact line stops moving. Note that the force diagrams in the insets of Fig. 22 (as well as all subsequent insets in Fig. 24-28 and 30) show only the net pinning force (yellow arrow) acting on the contact line, which should not be confused with the total net force. Of course, the total net force (with components from the spreading force and this pinning force) is always zero as long as the contact line is pinned. Note that the location of the right contact line pinning at t = 108 ps is on the surface of the graphene nanopillar (as opposed to on the bare hydrophilic substrate). At this particular condition, when the contact line is on the nanopillar, the contact is under two different forces (the forces that result in pinning) – the attractive force from both the graphene nanopillar and hydrophilic substrate (blue arrow) and the attractive force from just the hydrophilic substrate (green arrow). Of course, here the hydrophilic substrate is separated from the contact line by a distance of one graphene layer. As a result, the attractive force from just the hydrophilic substrate is slightly weaker than the attractive force of the gold-supported graphene monolayer despite the fact that gold is more hydrophilic than the gold-supported graphene monolayer. Accordingly, the net pull on the contact line is opposite to the direction of spreading, thereby pinning the contact line. Therefore, fundamental to this pinning is the fact that the contact line is at the junction of two surfaces of distinctly different wettability[60,61] as well as the fact that the nanopillar structure[62] introduces a graphene-layer-length separation distance from the gold surface.

While the right contact line continues to remain pinned, the left contact moves outward until it too becomes pinned at t = 225 ps. Interestingly, this pinning occurs on the hydrophilic substrate (as shown in the inset) rather than on the upper surface of the

graphene nanopillar. Here, the hydrophilic surface is no longer separated from the contact line by a distance of one graphene layer. Therefore, the attractive force from the gold (red arrow) supersedes the attractive force from graphene (blue arrow) since bare gold is more hydrophilic than the gold-supported graphene monolayer, and this pins the contact line by opposing the spreading force.

The right contact line, which has remained pinned from t = 108 ps, depins at t = 456 ps. This depinning indicates that the resistive pinning force has weakened and is no longer capable of balancing the spreading force. This occurs as some randomly fluctuating water molecules escape the pinned region and move nearer to the adjacent hydrophilic layer; as a result, all water molecules of the pinned zone are no longer separated from the more hydrophilic substrate by the one-graphene-layer distance. Consequently, the net attractive force becomes substantially reduced (or perhaps even reverses direction) so that the spreading force can no longer be balanced by the pinning force, and the drop subsequently spreads. Additionally, thermal fluctuations may cause a momentary increase in the contact angle while the contact line is being pinned; this increase in contact angle would lead to an enhanced spreading force resulting from the change in magnitude of the horizontal component of F_{LV}, thereby allowing the spreading force to overcome the resistive pinning force and initiate depinning.

However, at t = 516 ps, the right contact line again becomes pinned, this time on the hydrophilic surface, due to the stronger attractive force from the hydrophilic substrate as compared to the monolayer graphene nanopillar. The simulation proceeds for more time (ending at t = 1000 ps), but no further depinning of either contact line is observed. Therefore, one can infer that the spreading occurs in a combination of pinning-depinning

steps with the drop equilibrating upon the final pinning of both the left and right contact lines. This pinning results in an equilibrium drop configuration having a contact angle (≈72°) much larger than its theoretically-predicted Wenzel state value (≈50°).

4.2.2 2-layer Graphene Nanopillars on Bare Hydrophilic Substrate

Fig. 24 provides the snapshots of the MD-simulated nanodrop spreading dynamics for 2-layer graphene nanopillars on a bare hydrophilic substrate.

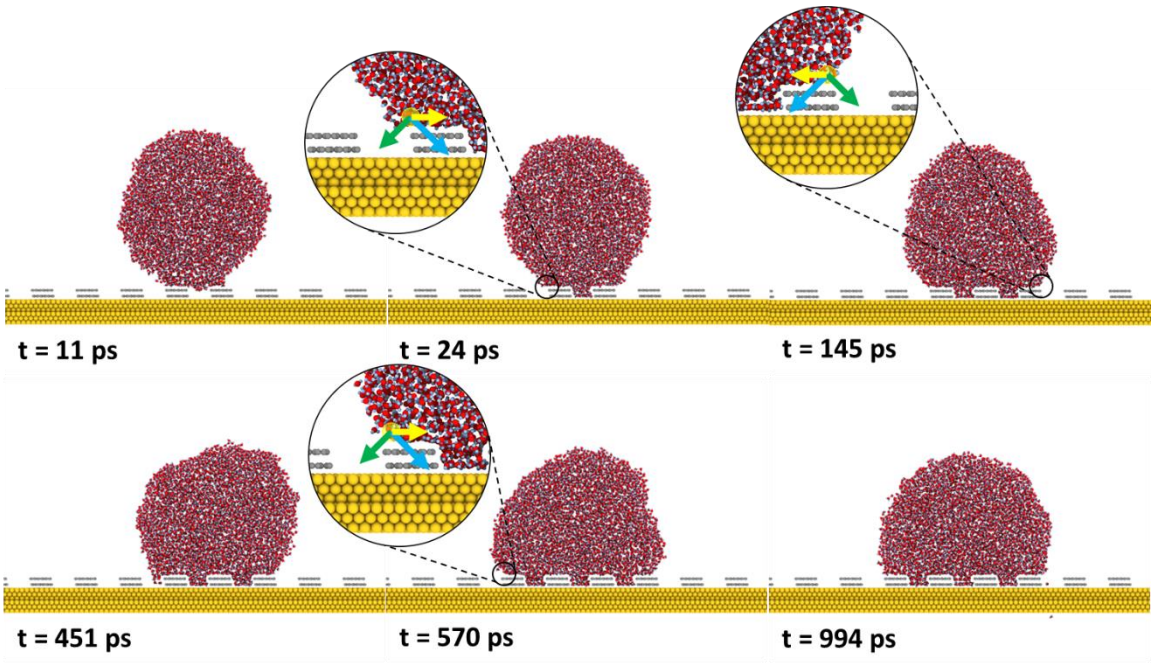

Figure 24: Snapshots of drop spreading for 2-layer graphene nanopillars on a bare hydrophilic substrate

Just like the previous case, here too all four forces (depicted in Fig. 23) are in action upon the onset of spreading. In this case, the left contact line is first pinned on the graphene nanopillar at t = 24 ps; again, the corresponding inset shows the attractive forces from the graphene nanopillars and gold substrate as well as the resulting pinning force. Wetting translucency implies that the gold-supported graphene bilayer (having a water drop contact angle of ≈90°) is less hydrophilic than a gold-supported graphene monolayer (having a water drop contact angle of ≈75°). Despite this, the attractive force from the graphene (blue

arrow) supersedes that from the gold (green arrow) since the contact line is separated from the gold by a distance of two graphene layers. As a consequence, the contact line on the graphene nanopillar experiences a retarding force large enough to oppose the spreading force, ensuring that the pinning occurs on the upper surface of the graphene nanopillar.

With the left contact line pinned, the right contact line continues to move until it too becomes pinned at t = 145 ps. Once again, the pinning occurs on the upper surface of the graphene nanopillar for the exact same reason described above.

At t = 451 ps, the left contact line, which has remained pinned since t = 24 ps, depins. Just like for the depinning of 1-layer graphene nanopillars, here too the depinning is initiated by water molecules randomly escaping from the pinned zone and wetting the adjacent hydrophilic layer, which in turn decays the pinning force so that it can no longer balance the spreading force.

Finally, the left contact line becomes pinned on the graphene nanopillar at t = 570 ps. No further depinning is witnessed for the remainder of the simulation (ending at t = 1000 ps). Therefore, here too the spreading occurs by a pinning-depinning procedure, and the final equilibrium is attained with both contact lines pinned. This equilibrium situation leads to a large, superhydrophobic contact angle (≈121°), introducing a new Wenzel state due to the fact that a transition from hydrophilic to hydrophobic regime is witnessed as the effective roughness increases (*i.e.*, the number of graphene layers comprising the nanopillar increases from one to two).

Note that for n = 2, the pinning force is larger than for n = 1, which is the reason that the drop equilibrates to a much greater contact angle. Such a large pinning force can be explained by the fact that the pinning always occurs at the graphene nanopillars with

the contact line being a distance of two graphene layers away from the hydrophilic gold. Therefore, the influence that may disturb the pinning, namely the attractive force from the gold, is weaker for n = 2 as compared to n = 1. Accordingly, the pinning force is substantially larger and can balance a larger spreading force, *i.e.*, a spreading force that corresponds to a much larger dynamic contact angle. Thus, pinning ensures attainment of equilibrium at this larger dynamic contact angle – this dynamic contact angle is then the equilibrium contact angle, which is substantially large and hydrophobic.

4.2.3 3-layer Graphene Nanopillars on Bare Hydrophilic Substrate

Figure 25 shows the drop dynamics on 3-layer graphene nanopillars on a bare hydrophilic substrate.

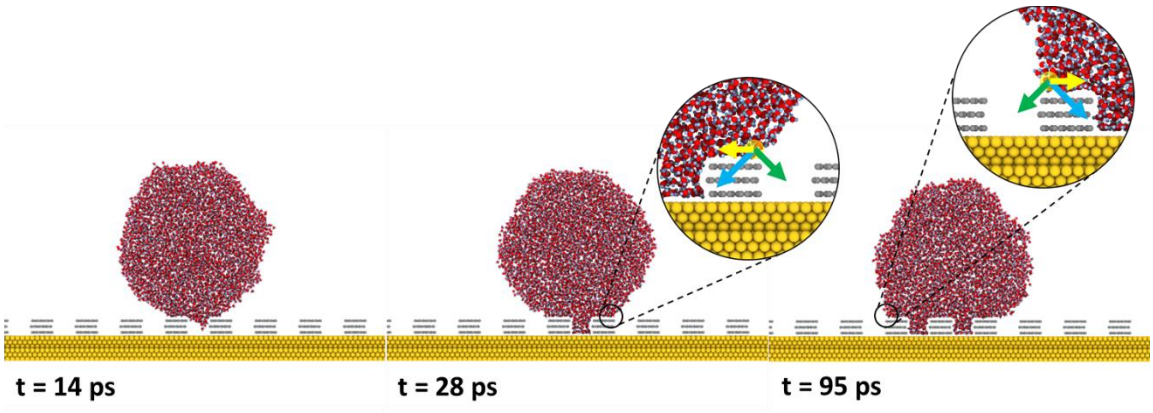

Figure 25: Snapshots of drop spreading for 3-layer graphene nanopillars on a bare hydrophilic substrate

Here, the right contact line gets pinned on a graphene nanopillar at t = 28 ps, and the left contact line gets pinned, also on a graphene nanopillar, at t = 95 ps. Similar to the previous case with 2-layer graphene nanopillars, the location of the contact line pinning is at the upper surface of graphene nanopillars due to the weaker attractive force of the hydrophilic surface, which results from the large separation distance between the contact line and the bare gold substrate at that location. However, unlike for 2-layer graphene nanopillars, in

this case there is no depinning witnessed after the initial pinnings for the entirety of the 1000 ps total simulation time. This implies a much larger pinning force in action, for the same reasons described in the previous section, which explains the attainment of a very large equilibrium contact angle (≈138°).

4.2.4 1-layer Graphene Nanopillars on Monolayer Graphene Supported by a Hydrophilic Substrate

In Fig. 26, snapshots of the drop spreading dynamics are shown for 1-layer graphene nanopillars on a monolayer of smooth (*i.e.*, non-perforated) graphene supported by a hydrophilic substrate.

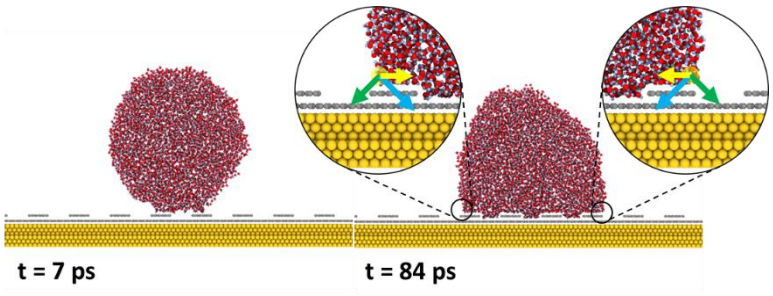

Figure 26: Snapshots of drop spreading for 1-layer graphene nanopillars on monolayer graphene supported by a hydrophilic substrate

Here, both the right and left contact lines are observed to pin simultaneously at t = 84 ps on the graphene nanopillars, and no depinning occurs for the remainder of the 500 ps simulation. Therefore, the drop equilibrates with such pinned contact lines, enforcing a large equilibrium contact angle. The fundamental question arising here is: why does pinning occur despite there being graphene nanopillars on monolayer graphene? This question is motivated by the fact that one would expect to see pinning for the case where the contact line is at a junction of two different materials of different wettabilities (*e.g.*, graphene nanopillars on bare gold as shown by Fig. 22, 24, and 25), while in this case the configuration is graphene on graphene. However, the pinning in this case can be attributed

to the wetting translucency property of graphene. This effect ensures that the contact angle on the graphene nanopillar should be larger as compared to the underlying graphene monolayer. Recall from Section 3.1 and Fig. 10 that the equilibrium contact angle on homogeneous *N*-layer graphene supported a hydrophilic gold substrate is ≈75° for $N = 1$ and ≈90° for $N = 2$. Hence, there is indeed a wettability jump at the edge of the nanopillar in this case as well; it is this jump that triggers the pinning force stemming from unequal attractive forces on the contact line from the nanopillar and the underlying graphene monolayer, as shown in the insets in Fig. 26. Of course, here the attractive force should be stronger from the nanopillar given that there is less of a difference in the hydrophilicity between gold-supported mono- and bilayer graphene and the underlying graphene is at a separation distance of one graphene layer from the contact line. This explains the pinning of both contact lines on the graphene nanopillars. Therefore, this particular case demonstrates how the wetting translucency of graphene interplays with the presence of nanopillars to induce contact line pinning and hence a superhydrophobic behavior with equilibrium contact angle of ≈122°. Of course, this superhydrophobic state can be considered as a new Wenzel state since gold-supported monolayer graphene is hydrophilic ($\theta \approx 75°$) and the presence of roughness of the same material (graphene) leads to hydrophobicity. The conversion from hydrophilic to hydrophobic regime with an increase in roughness is not possible in the classical Wenzel scenario.

4.2.5 2-layer Graphene Nanopillars on Monolayer Graphene Supported by a Hydrophilic Substrate

Fig. 27 illustrates the spreading on 2-layer graphene nanopillars deposited on a graphene monolayer supported by a hydrophilic substrate.

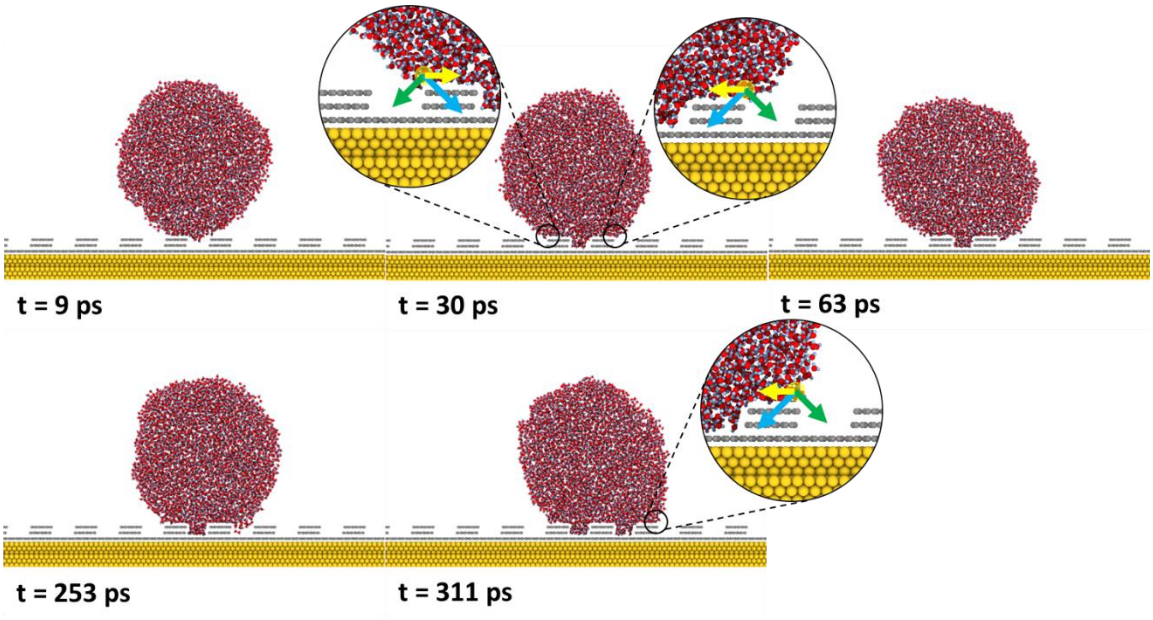

Figure 27: Snapshots of drop spreading for 2-layer graphene nanopillars on monolayer graphene supported by a hydrophilic substrate

Both contact lines become pinned virtually simultaneously (at t=30 ps), and as expected, the pinning occurs on the graphene nanopillars. However, unlike the previous case, here the right contact line releases some water molecules via molecular motion that wet the adjacent gold-supported graphene monolayer. This, in turn, reduces the pinning force, thereby initiating depinning of the contact line at t = 253 ps; this suggests that here the initial pinning is not as stable as for the previous case. However, the depinned contact line again gets pinned at t = 311 ps, and from this time onward, no further depinning is observed. Hence, with both contact lines pinned, the drop attains an equilibrium with a superhydrophobic contact angle of ≈150°. Furthermore, in this case the contact line motion occurs via a pinning-depinning mechanism, with the entire pinning process occurring as a consequence of the graphene wetting-translucency-induced wettability jump across the nanopillars as previously described. Fig. 22-27 establish that the graphene nanopillars

indeed provide a new route to achieve remarkable superhydrophobicity by the attainment of new Wenzel-like states caused by wettability-jump-induced pinning effects.

4.3 Cassie-Baxter State

In Fig. 28, the drop dynamics are provided for 4-layer graphene nanopillars on a bare hydrophilic substrate. For this system, the drop attains the CB state at equilibrium. During the spreading, the right contact line of the drop becomes pinned at t = 21 ps, virtually instantly after it contacts the pillars. On the other hand, the left contact line is not pinned but rather slides along the pillar, as can be seen in the snapshot for t = 105 ps. Note that this sliding motion occurs without wetting any part of the nanopillar other than the upper surface. At t = 180 ps, the left contact line becomes pinned, and no depinning occurs for the duration of the simulation (total time of 500 ps). Therefore, this is the equilibrium configuration of the drop with both contact lines pinned, resulting in the CB contact angle of ≈148° that is appreciably greater than that predicted by theory (≈122°).

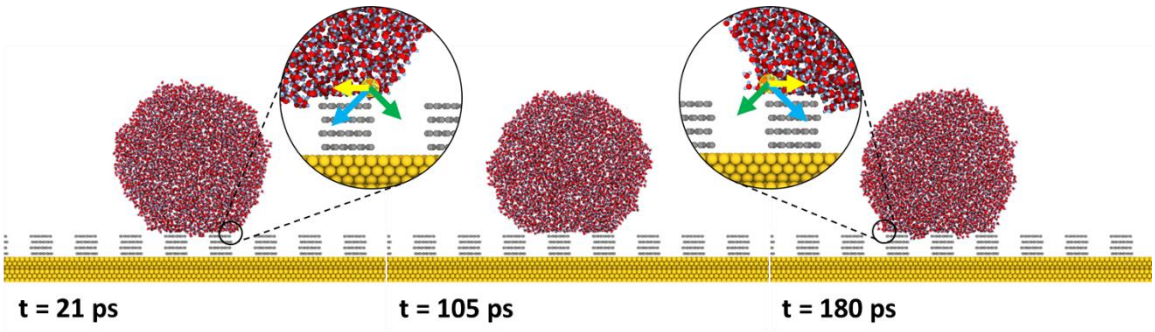

Figure 28: Snapshots of drop spreading for 4-layer graphene nanopillars on a bare hydrophilic substrate

Fig. 29 shows the temporal evolution of the advancing contact angle. As evident from Fig. 28, the right contact line is pinned nearly instantaneously after the drop is deposited, but the left contact moves. The advancing contact angle is the contact angle made by this advancing contact line with the horizontal upper surface of the graphene

nanopillars, as illustrated in Fig. 29. It is found that the spreading of this contact line to the adjacent nanopillar occurs as sliding. This is characterized by the liquid surface bending down and touching the face of the adjacent nanopillar, quantified by a progressive increase of this advancing contact angle for t = 20-100 ps. Very recently, Schellenberger *et al.* reported such a behavior for advancing water drops on superhydrophobic surfaces[63]; here that phenomenon is established for nanoscale systems through MD simulations. Once the advancing contact line has slid to the adjacent nanopillar, a steep decrease in the advancing contact angle is witnessed around $t \approx$ 110-115 ps because the drop no longer bends down but rather wets the next nanopillar surface – this is also identified in the experimental study[63].

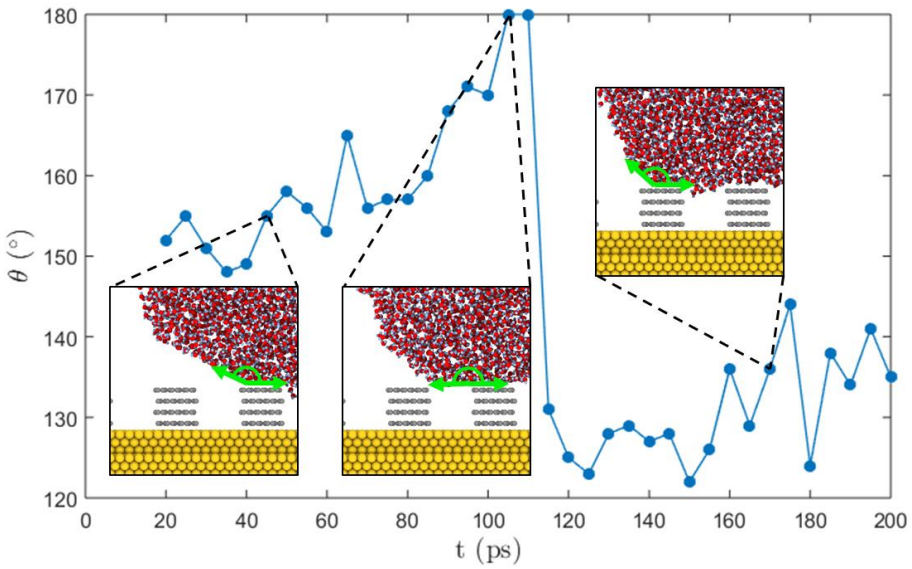

Figure 29: CB spreading dynamics – variation of dynamic (left) contact angle vs. time for 4-layer graphene nanopillars on a bare hydrophilic substrate

In Fig. 30, the spreading snapshots are shown for 3-layer graphene nanopillars on monolayer graphene supported by a hydrophilic substrate. This is also a case for which the drop attains a CB equilibrium state. The equilibrium CB contact angle is measured as ≈146°, which exceeds the predicted theoretical value of ≈122°.

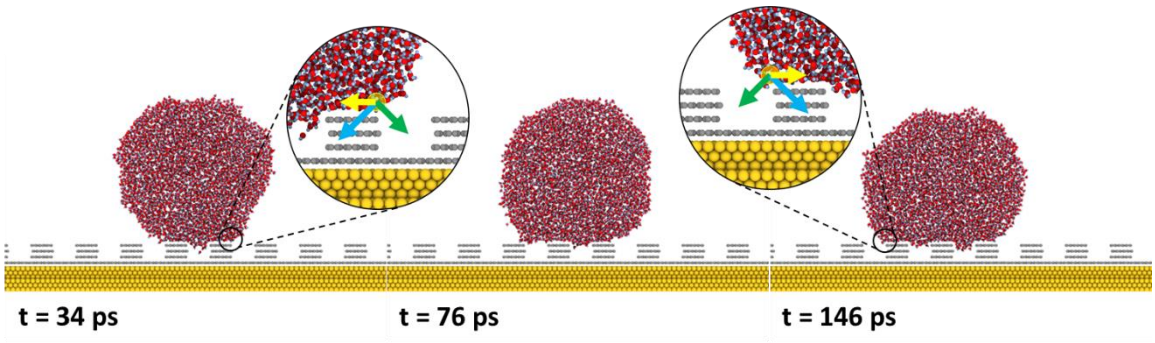

Figure 30: Snapshots of drop spreading for 3-layer graphene nanopillars on monolayer graphene supported by a hydrophilic substrate

With regards to the spreading dynamics, here again, the right contact line gets pinned almost immediately after contacting the graphene nanopillars, in this instance at t = 34 ps. Fig. 31 shows the temporal evolution of the advancing contact angle. As can be seen by comparing Fig. 31 to Fig. 29, essentially the same advancing left contact line and contact angle behavior is observed as for the previous case of 4-layer graphene nanopillars on bare gold. The left contact line slides along the upper nanopillar surface; correspondingly, the advancing contact angle first increases to ≈180° before decreasing sharply at $t \approx$ 80-85 ps.

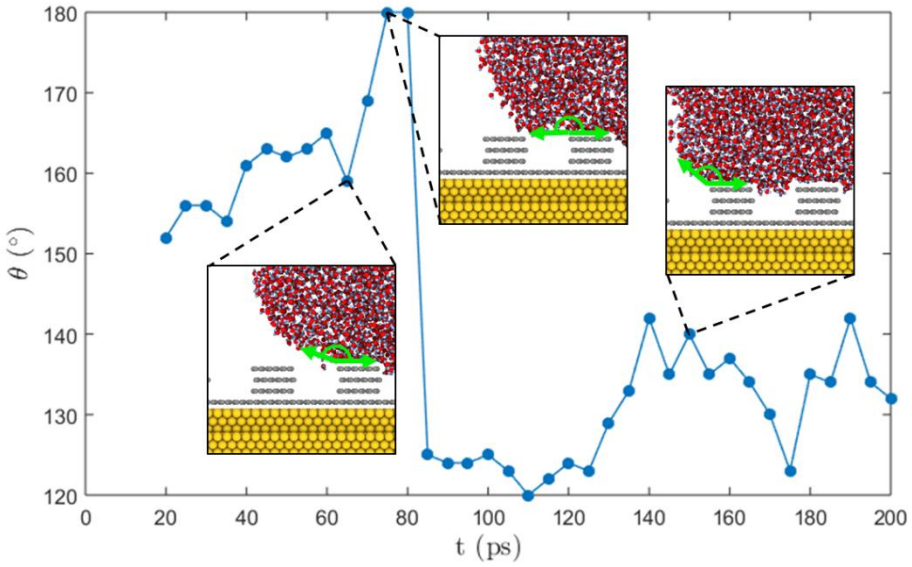

Figure 31: CB spreading dynamics – variation of dynamic (left) contact angle vs. time for 3-layer graphene nanopillars on monolayer graphene supported by a bare hydrophilic substrate

Hence, Fig. 28-31 unravel the mechanism by which the contact line advances on nanopillars in a CB wetting state, finding that the drop edge near the contact line actually bends down toward the adjacent nanopillar prior to wetting it. Commensurate with this bending is the momentary attainment of a very large dynamic contact angle of ≈180° followed by a steep decrease as the contact line jumps from one nanopillar to the next.

Chapter 5: Conclusions and Future Scope

The results of this work shed new light on the behavior of water drops as they wet graphene and graphene-coated substrates. As described in Chapter 3, MD simulations are employed to probe the wetting of water nanodrops on both hydrophobic and hydrophilic substrates having a smooth coating of graphene of varying number of layers. First, an analysis of the equilibrium contact angles attained through the MD simulations corroborates previous reports indicating that graphene exhibits wetting translucency characteristics. This wetting translucency effect is attributed to graphene's extreme thinness; when deposited onto a more hydrophilic substrate, the strength of water–hydrophilic-substrate vdW interactions are partially, but not completely, reduced, leading to an equilibrium contact angle intermediate to the substrate's hydrophilic contact angle and graphene's moderately hydrophobic contact angle. Second, the MD simulations allow for a molecular-level examination of the initial drop contact with the solid surface, which would not be possible in traditional wetting experiments. It is found that prior to the formation of a continuous liquid phase on the solid surface, patches of water molecules form on the surface around the contact location. These patches, representing the discrete, molecular nature of the liquid, eventually coalesce, signifying the transition to the continuous phase and the onset of the spreading process. Furthermore, the results of the patch formation analysis demonstrate that the transition from the discrete to continuous phase is tied directly to the strength of the water–solid interactions; stronger water–solid interactions promote enhanced patch formation and lead to the quicker attainment of a more uniform patch. Equivalently, the liquid attains the continuous phase in less time for stronger water–solid interactions. Third, the simulation results show that water drop spreading

dynamics on graphene universally obey a $r \sim t^{1/2}$ relationship. This is identical to the spreading of arbitrary LJ nanodrops on standard, non-layered solids, suggesting that unlike for the wetting statics, graphene's wetting translucency property is not reflected in the spreading dynamics. Finally, by looking into the timescales associated with spreading in the inertial and viscous regimes, it is shown that the capillary timescale is the relevant timescale for the spreading process observed in the MD simulations, indicating that the spreading occurs nearly entirely in the inertial regime.

Following the study of wetting on smooth graphene, further MD simulations are carried out to investigate the wetting of water nanodrops on hydrophilic substrates having surface roughness in the form of graphene nanopillars, as detailed in Chapter 4. First, it is found that the equilibrium contact angles for water drop wetting on systems with graphene nanostructure are much greater than those predicted by analytical theory. The equilibrium contact angles from the MD simulations exceed the predictions of both Wenzel and CB theory for graphene nanopillars on a bare hydrophilic substrate and graphene nanopillars on monolayer graphene supported by a hydrophilic substrate. Most remarkably, the results show for both cases that an increase in the roughness (achieved by increasing the number of graphene layers comprising the nanopillars) leads to a transition in the Wenzel state from a hydrophilic to hydrophobic wetting regime. Such a transition is not possible in classical Wenzel theory, suggesting that the observed wetting actually occurs in a new Wenzel-like state that is hitherto unreported in literature. Second, the mechanism responsible for these very large contact angles is elucidated. The wetting dynamics results reveal that the spreading occurs as a series of pinning-depinning steps. This pinning is attributed to the development of a pinning force that arises from the unequal attractive forces of the

graphene nanopillar and underlying substrate on the contact line (more appropriately, on a finite mass of liquid near the contact line) at the edge of the nanopillars. This pinning force, which acts to resist the spreading force and induce much larger equilibrium contact angles than predicted, is the result of the interplay between the geometrical configuration of the graphene nanopillars and the wetting-translucency-induced wettability gradient across the nanopillars. Third, a detailed analysis of the drop spreading in the CB state is performed. The results point to the mechanism by which the contact line is able to jump to an adjacent nanopillar when spreading in the CB state. Upon reaching the outer edge of a nanopillar, the edge of the drop bends down near the contact line, which is reflected in an increase of the advancing contact angle to ≈180°. Following this, the advancing contact line slides over to the adjacent nanopillar, and the advancing contact angle correspondingly decreases almost immediately.

In summary, these findings address two key questions about the wetting of graphene dictated by its remarkable wetting translucency property. Chapter 3 elucidates for the first time the effect of wetting translucency on spreading dynamics, and Chapter 4 illuminates the interplay of wetting translucency and geometrical structure for the realization of superhydrophobic graphene-based materials. These results are promising and point to a more facile route toward tailoring the wettability of graphene without compromising its chemical composition. Further inquiry into this interplay between wetting translucency and nanostructure may help quantify the effect of the nanostructure configuration on the wetting statics and dynamics. In particular, a comprehensive study of the effect of the nanostructure shape, size, and spacing may reveal systems having water drop contact angles even greater than those observed in this study.

Finally, the results of this work may serve as a basis and motivation for similar studies of other 2D materials, which extend beyond just graphene. For example, hexagonal boron nitride (h-BN), a 2D hexagonal arrangement of alternating boron and nitrogen atoms, has a similar structure to graphene but differing electronic properties[64]. Investigations into possible wetting translucency characteristics of h-BN and wetting-translucency-mediated contact line pinning on nanostructured h-BN surfaces may unlock new potential applications for h-BN or h-BN–graphene composite structures.

Appendix A: Derivation of Wenzel and Cassie-Baxter Wetting States

Consider a water drop wetting 1-layer graphene nanopillars on a bare hydrophilic (*i.e.*, gold) substrate as shown in Fig. 32. This spreading, which eventually leads to an equilibrium Wenzel state as detailed in Section 4.1, implies the creation (destruction) of a solid–liquid (solid–vapor) interface of area $A_1 + A_2 + A_3$ as well as the creation of a liquid–vapor interface of area A_{LV}. Let A_1 be defined as the area of the upper (horizontal) surface of the graphene nanopillar in contact with the water, A_2 as the area of the bare hydrophilic substrate in contact with the water, and A_3 as side (vertical) area of the graphene nanopillar in contact with the water, as illustrated in Fig. 32. Equilibrium is attained by minimizing the energy; consequently, it is possible to write

$$dE = A_1(\gamma_{SL,1} - \gamma_{SV,1}) + A_2(\gamma_{SL,2} - \gamma_{SV,2}) + A_3(\gamma_{SL,3} - \gamma_{SV,3}) + A_{LV}\gamma_{LV} = 0, \tag{A.1}$$

where γ_{ij} is the surface energy between phases i and j. The area of the additional liquid–vapor interface (A_{LV}) is related to the equilibrium Wenzel contact angle (θ_W) by

$$A_{LV} = (A_1 + A_2)\, cos(\theta_W). \tag{A.2}$$

Additionally, γ_{SL} and γ_{SV} can be related to γ_{LV} by Young's equation as[20]

$$\gamma_{SV} - \gamma_{SL} = \gamma_{LV}\, cos(\theta_i), \tag{A.3}$$

where θ_i is the equilibrium contact angle on the equivalent smooth surface. Substituting Eq. A.2 and A.3 into Eq. A.1 and simplifying yields

$$cos(\theta_W) = \frac{\sum_{i=1}^{n+2} A_i\, cos(\theta_i)}{A_1 + A_2}, \tag{A.4}$$

for the equation of the predicted Wenzel contact angle having n-layer graphene monopillars.

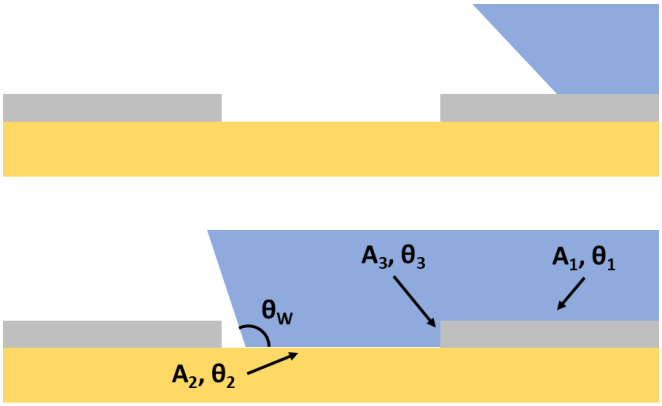

Figure 32: Schematic of drop spreading in Wenzel state for 1-layer graphene nanopillars on a bare gold substrate

This analysis is easily extended for the cases of 2- and 3-layer graphene nanopillars by accounting for the areas of the additional side surfaces with corresponding equilibrium contact angles on smooth versions of those surfaces, as shown in Fig. 33.

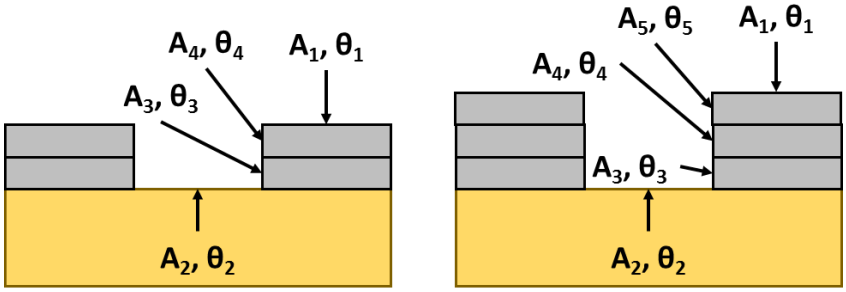

Figure 33: Schematic showing additional areas and contact angles associated with n-layer graphene nanopillars

Here, the width of the nanopilllars is equal to the spacing between them; that is, $A_1 = A_2 =$ 13 Å. Additionally, $A_3 = 3.31$ Å and $A_4 = A_5 = 3.355$ Å (see Section 2.4). It is evident that the wettability gradient across the graphene nanopillars, which arises due to graphene's wetting translucency property, implies that $\theta_3 \neq \theta_4 \neq \theta_5 \neq \theta_1$. Thus, there is not an immediately obvious choice for the values of θ_3, θ_4, and θ_5, so they are simply approximated as the mean of the equilibrium contact angles of the upper and lower faces corresponding to surfaces A_3, A_4, and A_5, respectively. The equilibrium contact angle values

for *N*-layer smooth (i.e., non-perforated) graphene supported by a bare hydrophilic substrate (from MD simulation) are given in Table 4.

Table 4: Equilibrium contact angle values for N-layer smooth graphene supported by a bare hydrophilic substrate

Number of Graphene Layers (*N*)	Equilibrium Contact Angle ($\theta_{eq,N}$)
1	75.2°
2	91°
3	90.6°
4	94.1°

Using these values, θ_3, θ_4, and θ_5 are approximated as

$$\theta_3 = \frac{1}{2}\left(\theta_{eq,1} + \theta_2\right) \tag{A.5}$$

$$\theta_4 = \frac{1}{2}\left(\theta_{eq,2} + \theta_{eq,1}\right) \tag{A.6}$$

$$\theta_5 = \frac{1}{2}\left(\theta_{eq,3} + \theta_{eq,2}\right), \tag{A.7}$$

which are then substituted in Eq. A.4 to determine the predicted contact angle values for wetting in the classical Wenzel state. The calculated values are summarized in Table 5.

The CB state is attained for 4-layer graphene nanopillars on the bare gold surface. Energy minimization leads to[20]

$$cos(\theta_{CB}) = \phi_s\, cos(\theta_1) + (\phi_s - 1), \tag{A.8}$$

where θ_{CB} is the predicted contact angle in the CB state, θ_1 is the contact angle at the upper surface of the 4-layer graphene nanopillar, and ϕ_s is the void fraction, which here equals 0.5 because $A_1 = A_2$. The predicted CB contact angle value is included in Table 5.

Table 5: Predicted contact angle values for n-layer graphene nanopillars on bare gold

Number of Layers in the Graphene Nanopillars (n)	Predicted Contact Angle (θ_W or θ_{CB})
1	50.1°
2	58.6°
3	58.5°
4	122.4°

The preceding analysis can also be carried out for the cases of wetting of n-layer graphene nanopillars on smooth monolayer graphene supported by a hydrophilic substrate. The fully-wetted Wenzel state is attained for n = 1 and 2. In this case, the formulation of Eq. A.4 is exactly the same, except that A_2 and θ_2 now correspond not to the bare hydrophilic gold surface but rather the gold-supported monolayer graphene surface. The CB state is attained for n = 3; hence, Eq. A.8 is applicable for this case. The predicted Wenzel and CB contact angle values for n-layer graphene nanopillars on a gold-supported graphene monolayer are summarized in Table 6.

Table 6: Predicted contact angle values for n-layer graphene nanopillars on a gold-supported graphene monolayer

Number of Layers in the Graphene Nanopillars (n)	Predicted Contact Angle (θ_W or θ_{CB})
1	82.3°
2	82.2°
3	122.4°

References

1. Novoselov, K. S. *et al.* Electric Field Effect in Atomically Thin Carbon Films. *Science* **306,** 666–669 (2004).

2. Stankovich, S. *et al.* Graphene-based composite materials. *Nature* **442,** 282–286 (2006).

3. Nair, R. R. *et al.* Fine Structure Constant Defines Visual Transperency of Graphene. *Science* **320,** 1308 (2008).

4. Aghigh, A. *et al.* Recent advances in utilization of graphene for filtration and desalination of water: A review. *Desalination* **365,** 389–397 (2015).

5. Han, Y., Xu, Z. & Gao, C. Ultrathin Graphene Nanofiltration Membrane for Water Purification. *Adv. Funct. Mater.* **23,** 3693–3700 (2013).

6. Mahmoud, K. A., Mansoor, B., Mansour, A. & Khraisheh, M. Functional graphene nanosheets: The next generation membranes for water desalination. *Desalination* **356,** 208–225 (2015).

7. Surwade, S. P. *et al.* Water desalination using nanoporous single-layer graphene. *Nat. Nanotechnol.* **10,** 459–464 (2015).

8. Lu, X., Wang, X., Jin, J., Zhang, Q. & Chen, J. Electrochemical biosensing platform based on amino acid ionic liquid functionalized graphene for ultrasensitive biosensing applications. *Biosens. Bioelectron.* **62,** 134–139 (2014).

9. Zhang, J., Lei, J., Pan, R., Xue, Y. & Ju, H. Highly sensitive electrocatalytic biosensing of hypoxanthine based on functionalization of graphene sheets with water-soluble conducting graft copolymer. *Biosens. Bioelectron.* **26,** 371–376 (2010).

10. Yin, J. *et al.* Generating electricity by moving a droplet of ionic liquid along graphene. *Nat. Nanotechnol.* **9,** 378–383 (2014).

11. Park, S. *et al.* Design of graphene sheets-supported Pt catalyst layer in PEM fuel cells. *Electrochem. commun.* **13,** 258–261 (2011).

12. Song, B. *et al.* Water-dispersible graphene/polyaniline composites for flexible micro-supercapacitors with high energy densities. *Nano Energy* **16,** 470–478 (2015).

13. Marmur, A. The Lotus Effect: Superhydrophobicity and Metastability. *Langmuir* **20,** 3517–3519 (2004).

14. Gao, X. & Jiang, L. Water-repellent legs of water striders. *Nature* **432,** 36–36 (2004).

15. Fürstner, R., Barthlott, W., Neinhuis, C. & Walzel, P. Wetting and Self-Cleaning Properties of Artificial Superhydrophobic Surfaces. *Langmuir* **21,** 956–961 (2005).

16. Rothstein, J. P. Slip on Superhydrophobic Surfaces. *Annu. Rev. Fluid Mech.* **42,** 89–109 (2010).

17. Zhu, Q., Pan, Q. & Liu, F. Facile Removal and Collection of Oils from Water Surfaces through Superhydrophobic and Superoleophilic Sponges. *J. Phys. Chem. C* **115,** 17464–17470 (2011).

18. Miljkovic, N. & Wang, E. N. Condensation heat transfer on superhydrophobic surfaces. *MRS Bull.* **38,** 397–406 (2013).

19. Miljkovic, N., Preston, D. J., Enright, R. & Wang, E. N. Jumping-droplet electrostatic energy harvesting. *Appl. Phys. Lett.* **105,** 013111 (2014).

20. de Gennes, P.-G., Brochard-Wyart, F. & Quere, D. in *Capillarity and Wetting Phenomena: Drops, Bubbles, Pearls, Waves* 215–258 (Springer, 2004).

21. Rafiee, J. *et al.* Wetting transparency of graphene. *Nat. Mater.* **11,** 217–222 (2012).

22. Shin, Y. J. *et al.* Surface-Energy Engineering of Graphene. *Langmuir* **26,** 3798–3802 (2010).

23. Raj, R., Maroo, S. C. & Wang, E. N. Wettability of Graphene. *Nano Lett.* **13,** 1509–1515 (2013).

24. Shih, C.-J., Strano, M. S. & Blankschtein, D. Wetting translucency of graphene. *Nat. Mater.* **12,** 866–869 (2013).

25. Winkels, K. G., Weijs, J. H., Eddi, A. & Snoeijer, J. H. Initial spreading of low-viscosity drops on partially wetting surfaces. *Phys. Rev. E* **85,** 055301 (2012).

26. Wang, J.-N. *et al.* Recent developments in superhydrophobic graphene and graphene-related materials: from preparation to potential applications. *Nanoscale* **7,** 7101–7114 (2015).

27. Lee, J.-S., Yoon, J.-C. & Jang, J.-H. A route towards superhydrophobic graphene surfaces: surface-treated reduced graphene oxide spheres. *J. Mater. Chem. A* **1,** 7312–7315 (2013).

28. Lin, Z., Liu, Y. & Wong, C. P. Facile fabrication of superhydrophobic octadecylamine-functionalized graphite oxide film. *Langmuir* **26,** 16110–16114 (2010).

29. Rafiee, J., Rafiee, M. A., Yu, Z. Z. & Koratkar, N. Superhydrophobic to Superhydrophilic Wetting Control in Graphene Films. *Adv. Mater.* **22,** 2151–2154 (2010).

30. Zhang, X., Wan, S., Pu, J., Wang, L. & Liu, X. Highly hydrophobic and adhesive performance of graphene films. *J. Mater. Chem.* **21,** 12251–12258 (2011).

31. Chen, Z., Dong, L., Yang, D. & Lu, H. Superhydrophobic Graphene-Based Materials: Surface Construction and Functional Applications. *Adv. Mater.* **25,** 5352–5359 (2013).

32. Zang, J. *et al.* Multifunctionality and control of the crumpling and unfolding of large-area graphene. *Nat. Mater.* **12,** 321–325 (2013).

33. Chen, P.-Y. *et al.* Multiscale Graphene Topographies Programmed by Sequential Mechanical Deformation. *Adv. Mater.* **28,** 3564–3571 (2016).

34. Plimpton, S. Fast Parallel Algorithms for Short–Range Molecular Dynamics. *J. Comput. Phys.* **117,** 1–19 (1995).

35. Stukowski, A. Visualization and analysis of atomistic simulation data with OVITO–the Open Visualization Tool. *Model. Simul. Mater. Sci. Eng.* **18,** 015012 (2010).

36. Frenkel, D. & Smit, B. in *Understanding Molecular Simulation* 63–107 (Academic Press, 2002).

37. Verlet, L. Computer 'Experiements' on Classical Fluids. I. Themrodynamical Properties of Lennard-Jones Molecules. *Phys. Rev.* **159,** 98–103 (1967).

38. Allen, M. P. & Tildesley, D. J. in *Computer Simulation of Liquids* 1–32 (Oxford University Press, 1987).

39. Shih, C.-J. *et al.* Breakdown in the Wetting Transparency of Graphene. *Phys. Rev. Lett.* **109,** 176101 (2012).

40. Orsi, M. Comparative assessment of the ELBA coarse-grained model for water. *Mol. Phys.* **112,** 1566–1576 (2014).

41. Ryckaert, J.-P., Ciccotti, G. & Berendsen, H. J. C. Numerical Integration of the Cartesian Equations of Motion of a System with Constraints: Molecular Dynamics of n-Alkanes. *J. Comput. Phys.* **23,** 327–341 (1977).

42. Hockney, R. W., Goel, S. P. & Eastwood, J. W. A 10000 Particle Molecular Dynamics Model with Long Range Forces. *Chem. Phys. Lett.* **21,** 589–591 (1973).

43. Sławińska, J., Dabrowski, P. & Zasada, I. Doping of graphene by a Au(111) substrate: Calculation strategy within the local density approximation and a semiempirical van der Waals approach. *Phys. Rev. B* **83,** 245429 (2011).

44. Giovannetti, G. *et al.* Doping Graphene with Metal Contacts. *Phys. Rev. Lett.* **101,** 026803 (2008).

45. Werder, T., Walther, J. H., Jaffe, R. L., Halicioglu, T. & Koumoutsakos, P. On the Water-Carbon Interaction for Use in Molecular Dynamics Simulations of Graphite and Carbon Nanotubes. *J. Phys. Chem. B* **107,** 1345–1352 (2003).

46. Wang, S., Zhang, Y., Abidi, N. & Cabrales, L. Wettability and surface free energy of graphene films. *Langmuir* **25,** 11078–11081 (2009).

47. Merabia, S. *et al.* Heat transfer from nanoparticles: a corresponding state analysis. *Proc. Natl. Acad. Sci. U. S. A.* **106,** 15113–15118 (2009).

48. Girit, Ç. Ö. *et al.* Graphene at the Edge: Stability and Dynamics. *Science* **323,**

1705–1708 (2009).

49. Jennings, A. T., Burek, M. J. & Greer, J. R. Microstructure versus Size: Mechanical Properties of Electroplated Single Crystalline Cu Nanopillars. *Phys. Rev. Lett.* **104,** 135503 (2010).

50. Jang, D., Li, X., Gao, H. & Greer, J. R. Deformation mechanisms in nanotwinned metal nanopillars. *Nat. Nanotechnol.* **7,** 594–601 (2012).

51. Nose, S. Constant-temperature molecular dynamics. *J. Phys. Condens. Matter* **2,** SA115–SA119 (1990).

52. van der Spoel, D., van Maaren, P. J. & Berendsen, H. J. C. A systematic study of water models for molecular simulation: Derivation of water models optimized for use with a reaction field. *J. Chem. Phys.* **108,** 10220–10230 (1998).

53. Das, S., Waghmare, P. R. & Mitra, S. K. Early regimes of capillary filling. *Phys. Rev. E* **86,** 067301 (2012).

54. Babu, J. S. & Sathian, S. P. The role of activation energy and reduced viscosity on the enhancement of water flow through carbon nanotubes. *J. Chem. Phys.* **134,** 194509 (2011).

55. Joseph, S. & Aluru, N. R. Why Are Carbon Nanotubes Fast Transporters of Water ? *Nano Lett.* **8,** 452–458 (2008).

56. Majumder, M., Chopra, N., Andrews, R. & Hinds, B. J. Enhanced flow in carbon nanotubes. *Nature* **438,** 44 (2005).

57. Xu, B. *et al.* Temperature dependence of fluid transport in nanopores. *J. Chem. Phys.* **136,** 184701 (2012).

58. Holt, J. K. *et al.* Fast Mass Transport Through Sub-2-Nanometer Carbon Nanotubes. *Science* **312,** 1034–1037 (2006).

59. Marchand, A., Weijs, J. H., Snoeijer, J. H. & Andreotti, B. Why is surface tension a force parallel to the interface? *Am. J. Phys.* **79,** 999–1008 (2011).

60. Wang, F.-C. & Wu, H.-A. Pinning and depinning mechanism of the contact line during evaporation of nano-droplets sessile on textured surfaces. *Soft Matter* **9,** 5703–5709 (2013).

61. Zhang, J., Müller-Plathe, F. & Leroy, F. Pinning of the Contact Line during Evaporation on Heterogeneous Surfaces: Slowdown or Temporary Immobilization? Insights from a Nanoscale Study. *Langmuir* **31,** 7544–7552 (2015).

62. Kalinin, Y. V., Berejnov, V. & Thorne, R. E. Contact Line Pinning by Microfabricated Patterns: Effects of Microscale Topology. *Langmuir* **25,** 5391–5397 (2009).

63. Schellenberger, F., Encinas, N., Vollmer, D. & Butt, H.-J. How Water Advances on Superhydrophobic Surfaces. *Phys. Rev. Lett.* **116,** 096101 (2016).

64. Song, L. *et al.* Large scale growth and characterization of atomic hexagonal boron nitride layers. *Nano Lett.* **10,** 3209–3215 (2010).